Impedance Modeling and Mechanism Analysis of Low-Frequency Oscillations in Single-Phase MMC-RPC Integrated Vehicle-Grid Coupling System

Pengkun Li, *Graduate Student Member, IEEE*, Yue Wang, *Member, IEEE*, Yi Liu, Quanle Zhu, Yinglin Xue, *Member, IEEE*, Xuan Li, *Member, IEEE*, Bole Feng, and Runtian Li

***Abstract*—The single-phase modular multilevel converter-based railway static power conditioner (MMC-RPC) has significant advantages in governing the power quality problems in the traction power supply system. The mechanism analysis of low-frequency oscillations (LFOs) in the MMC-RPC integrated vehicle-grid coupling system when electric multiple units are put into operation is a critical issue, which has been investigated in this article. The third-order ac admittance models of single-phase MMC-RPC and vehicle rectifiers are developed for the first time. To comprehensively study the small-signal stability of the MMC-RPC integrated vehicle-grid coupling system, this article proposes a modal analysis method based on modal phase margin and parameter sensitivity and combined with the generalized Nyquist stability criterion. It is found that LFOs around 10 Hz or 48 Hz are prone to occur due to the interactions of MMC-RPC or vehicle rectifiers with the traction power grid. To reveal the LFO mechanism, dominant modes and key parameters leading to LFOs in different working scenarios are clarified, and a series of guidelines are proposed for LFO elimination. Furthermore, the effects of control loops and power flow of MMC-RPC on system stability are revealed in detail. Finally, real-time hardware-in-the-loop experimental results validate the theoretical analysis.**

***Index Terms*—Impedance modeling, low-frequency oscillation, modal analysis, railway static power conditioner, single-phase modular multilevel converter, small-signal stability, vehicle-grid coupling system.**

I. Introduction

In RECENT years, electrified railways have played a significant role in increasing the speed and capacity of railway transportation [1]. To solve the power quality problems such as active power imbalance between phases, significant amount of negative-sequence currents, and low power factor in electric traction systems, scholars in Japan proposed an auxiliary device called railway static power conditioner (RPC) in 1993 [2]. It compensates reactive current and transfers energy within two phases to eliminate negative-sequence currents and ensure equal active power consumption and has been a promising device in electrified railways [3], [4], [5]. In traditional RPC, two- or three-level voltage source converters are connected back-to-back at the dc side and to the ac traction power grid through step-down transformers. However, traditional RPC has the defects of small capacity, large occupancy area, high cost, and low power quality, which reduce its performance [6]. With the increasing application of modular multilevel converter (MMC), the advantages of high power quality and large capacity are highlighted. Therefore, much research has been done applying single-phase MMC in RPC instead, which also brings the merits of eliminating step-down transformers and reducing energy losses [7], [8], [9].

With the high-density operation of electric multiple units (EMUs) and ac/dc/ac drive electric locomotives (hereafter called vehicles), the traction power system has become increasingly complex. The dynamic interactions between EMUs and the traction power grid become very serious, which results in a series of low-frequency oscillation (LFO) problems [10], [11], [12], [13]. On the other hand, research in three-phase or single-phase MMC-based systems indicates that complex internal couplings in submodules of MMC and interactions of the control systems might bring negative damping effects and induce oscillations in a wide frequency range [14]. Hence, it is worth studying the small-signal stability of the single-phase MMC-RPC integrated vehicle-grid coupling system in detail.

Two commonly used methods are developed for the system-level stability analysis: the eigenvalue-based method in the time domain and the impedance-based method in the frequency domain [15], [16]. Compared with the eigenvalue analysis, the superior feature of the impedance-based method is the black-box modeling, i.e., the impedance of converters and the electric network can be measured with the frequency sweeping technique. This feature is particularly attractive for analyzing the interactions of multiple converters provided by different vendors.

Manuscript received 27 June 2022; revised 22 September 2022 and 21 November 2022; accepted 24 December 2022. Date of publication 2 January 2023; date of current version 14 February 2023. This work was supported by Science and Technology Projects of State Grid Corporation of China under Grant 5100-202156434A-0-0-00. Recommended for publication by Associate Editor Y. Xue. *(Corresponding auhtor: Yue Wang.)*

Pengkun Li, Yue Wang, Yi Liu, Bole Feng, and Runtian Li are with the State Key Laboratory of Electrical Insulation and Power Equipment, Xi'an Jiaotong University, Xi'an 710049, China (e-mail: lipengkun@stu.xjtu.edu.cn; davidwangyue@mail.xjtu.edu.cn; 4121104089@stu.xjtu.edu.cn; fengbl@stu.xjtu.edu.cn; runtianli1998@stu.xjtu.edu.cn).

Quanle Zhu, Yinglin Xue, and Xuan Li are with the State Grid Economic and Technological Research Institute Co., Ltd., Beijing 102209, China (e-mail: zhuquanle@126.com; xueyinglin2022@163.com; lixuan@chinasperi.sgcc.com.cn).

Color versions of one or more figures in this article are available at https://doi.org/10.1109/TPEL.2022.3233350.

Digital Object Identifier 10.1109/TPEL.2022.3233350

Therefore, scholars have conducted in-depth research on the impedance-based small-signal stability analysis of vehicle-grid systems [17], [18], [19], [20], [21], [22], [23], [24], [25], [26], [27], [28]. DQ impedance models of four-quadrant rectifiers in vehicles were established to analyze the influence of system parameters, but the frequency coupling effects were ignored [17], [18], [19], [20], [21], [22]. A second-order impedance model of a single-phase rectifier in the sequence domain was developed in [23] based on the harmonic linearization method, but only mirror-frequency coupling effects between harmonics at frequencies f_p and f_p-$2f_1$ were taken into account, where f_p is the perturbation frequency and f_1 is the fundamental frequency. In fact, in single-phase converters, the complete frequency coupling effect is reflected between small-signal harmonics with the frequency of f_p and $f_p \pm 2f_1$. Moreover, the above literature assumed that the initial phase of the voltage at PCC is zero when modeling while ignoring the truth that the initial phase of the reference frame is always a nonzero value. Single-input single-output (SISO) impedance model and voltage loop model of the vehicle rectifiers were built in [24] and [25] to simplify the system stability analysis. An RLC circuit model was established in [26] to analyze the respective contribution of networks and locomotives to LFO. To deal with the situation when the detailed system parameters are unknown, Pan et al. [27] and Hu et al. [28] studied the train-network impedance measurement methods, which make up for the shortcomings of the existing research.

To suppress the LFOs in vehicle-grid systems, the latest literature mainly focused on grid enhancement, control algorithms optimization, and additional device placement [29], [30], [31], [32], [33], [34], [35], [36], [37], [38]. Autodisturbance rejection control, passivity-based control, and predictive control strategy were separately adopted in [30], [31], and [32] instead of PI control to increase system damping. Diode-bridge rectification mode is applied in [33] to reshape the impedance characteristics of rectifiers and mitigate LFOs online. *LC* and *LCL* high-pass filters were designed to reduce high-order harmonics in [34]. It is found in [35], [36], [37], and [38] that the access of static synchronous compensator (STATCOM) or active power filter (APF) in the traction system can improve system stability. Nevertheless, Liu et al. [35] did not explore the internal mechanism of system stability improvement effects brought by MMC-STATCOM but only proved it by simulation. The impacts of STATCOM and APF were compared in [37], and it was pointed out that the latter could provide more damping than the former. But the research on APF and STATCOM can only present qualitative results, such as stable or unstable, and cannot explicitly convey the compensator impacts [38]. The differences between the above-mentioned two compensators and the single-phase MMC-RPC studied in this article are reflected in all their power stage topologies, control algorithms, and functions of these compensators. Therefore, the stability of the vehicle-grid coupling system with the integration of single-phase MMC-RPC is a brand-new topic and is worthy of full investigation.

In the MMC-HVdc systems, many papers have established ac and dc impedance models of three-phase MMC and explored its interactive stability with the power grid or wind farms [39], [40]. However, the RPC studied in this article adopts single-phase MMC but not three-phase MMC. And there are great differences between single-phase and three-phase MMCs in the power stage, control system, and internal harmonic characteristics. The differences reflected in the power stage and the control system are obvious, thus are not explained here. For the harmonic characteristics, in symmetrical three-phase MMC, only positive-sequence and negative-sequence differential-mode (DM) steady-state current components at $(6k\pm1)\cdot f_1$ (k is an integer) will flow into the ac side. All zero-sequence common-mode (CM) components at $6k\cdot f_1$ will flow into the dc side. For an asymmetric three-phase system with unbalanced grid voltage, "a chain reaction" exists causing infinite many frequency couplings, which will be more complex and one may refer to [41] for a more detailed discussion. While in single-phase MMC, all DM components at $(2k\pm1)\cdot f_1$ will flow into the ac side and all CM components at $2k\cdot f_1$ will flow into the dc side. Similar differences exist in the small-signal harmonics, which are not expanded in detail here. Due to the above-mentioned differences, the admittance model of single-phase MMC-RPC cannot be developed directly from three-phase MMC and need to be rebuilt. Until now, most literature about single-phase MMC-RPC mainly paid attention to its control optimization [7], [8], [9], [42], [43], [44], [45]. Impedance modeling and stability analysis of the single-phase MMC-RPC integrated vehicle-grid coupling system has not been well addressed and needs further study, which is, thus, the focus of this article.

In the eigenvalue-based analysis method, eigenvalue loci of the coefficient matrix are often plotted to find out the instability modes and parameters, which may cause instability. Participation-factor method is then applied to weigh the participation of state variables. The sensitivity of parameters on the damping ratios of eigenvalues, which may move to the right-half plane is finally studied to evaluate the influence of parameters quantitatively [46]. However, in the impedance-based method, most literature only observes whether the amplitude-frequency curves have intersection points and whether the corresponding phase difference exceeds 180° for the SISO systems or the overall system stability margin for the multiple-input multiple-output (MIMO) systems is smaller than 0°, but did not extract enough relevant features of instability modes and also lacked quantitative evaluation of the effects of parameters. Especially for a single-phase system, the impedance matrix has higher orders when the complete coupling effects are considered. The influencing rules of parameters will be more complicated, e.g., the dominant mode may change and maybe more than one mode will cause harmonic instability. Therefore, the Nyquist stability analysis method needs to be expanded and enriched for parameter sensitivity analysis and key factors extraction. For SISO systems, Li et al. [47] raised a design-oriented small-signal stability analysis method based on resistance sensitivity and phase-difference sensitivity. For MIMO systems, imitating the participation-factor method in the eigenvalue-based method, participation functions were also defined in the impedance-based method to quantify the sensitivity of different converters to the stability of a multimachine interconnected system [48], [49], [50]. However, the research did not involve the sensitivity of

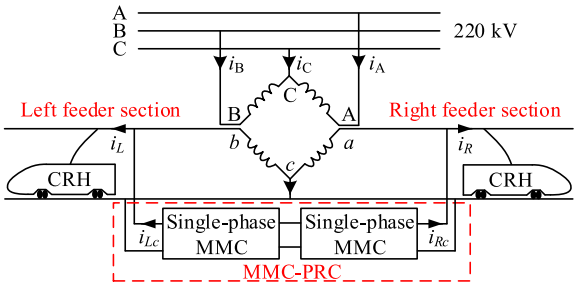

Fig. 1. Structure of the single-phase MMC-RPC integrated vehicle-grid coupling system.

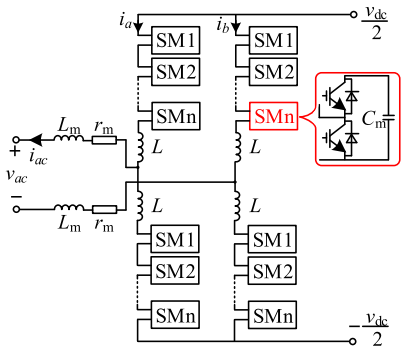

Fig. 2. Diagram of single-phase MMC adopted in the RPC.

specific system parameters and needs more reasonable indices to quantitatively evaluate system stability and the effects of system parameters.

To cope with the above-mentioned issues, the main contributions of this article are summarized as follows.

1) This article, for the first time, systematically studies the small-signal stability of the vehicle-grid coupling system with the integration of single-phase MMC-RPC. Accurate third-order ac admittance models of single-phase MMC-RPC and vehicle rectifiers with capturing multiharmonic characteristics are first developed. Furthermore, the effects of frequency coupling, grid impedance coupling, and the initial phase of the reference frame on the low-frequency band of ac admittances are explicitly elaborated.
2) A modal analysis method based on modal phase margin and parameter sensitivity is proposed combined with the generalized Nyquist stability criterion (GNC). Dominant modes, key control parameters, and key control loops of the single-phase MMC-RPC integrated vehicle-grid coupling system in different working scenarios are clarified. The proposed method is equally adapted to general MIMO cascade systems for stability analysis.
3) The mechanism of LFOs in the single-phase MMC-RPC integrated vehicle-grid coupling system is revealed, including the accurate estimation of stability boundary and oscillation frequency. A series of guidelines are summed up for LFO suppression. In addition, the stability change of the vehicle-grid system caused by the control loops and compensated power of MMC-RPC is further elucidated.

The rest of this article is organized as follows. Sections II and III develop the ac admittance models of the single-phase MMC-RPC and vehicle rectifiers. Section IV mainly studies the interaction stability of the single-phase MMC-RPC and traction power grid. Section V specifically explores the small-signal stability of the vehicle-grid coupling system with and without single-phase MMC-RPC. The real-time hardware-in-the-loop (HIL) experimental results are presented in Section VI. Finally, Section VII concludes this article.

II. AC Admittance Modeling of Single-Phase MMC-RPC

The structure of the single-phase MMC-RPC integrated vehicle-grid coupling system is shown in Fig. 1. The three-phase traction power grid forms two single-phase feeder sections through the unbalanced three-phase V/V transformer and supplies power to vehicles. RPC adopts two single-phase MMCs, which are connected back-to-back at the dc side and directly connected to two feeders at the ac side. Since the left and right feeder sections are symmetrical, this article will focus on the small-signal stability of the right part and explore its LFO mechanism. This section first develops the small-signal models of the power stage and control system of single-phase MMC-RPC and then derives its third-order ac admittance model based on the multiharmonic linearization method.

A. Steady-State and Small-Signal Modeling of Power Stage

As shown in Fig. 2, the single-phase MMC adopted in the RPC of this article has four arms, each consisting of N submodules (SMs). All SMs adopt the half-bridge topology here. C_{m} is the capacitance value of SM capacitors. L is the arm inductance. L_{m} and r_{m} are equivalent series inductance and resistance at the ac side, respectively. Assuming that all SM capacitor voltages are well balanced, the time-domain averaged model of the power stage of single-phase MMC-RPC can be expressed as

$$\begin{cases} 2L\dfrac{di_a}{dt} + 2L_m\dfrac{di_{\mathrm{ac}}}{dt} + 2R_m i_{\mathrm{ac}} = v_{\mathrm{dc}} - 2m_a v_a - v_{\mathrm{ac}} \\ C\dfrac{dv_a}{dt} = m_a i_a \end{cases} \tag{1}$$

where v_{dc} is the dc voltage. v_{ac} and i_{ac} are, respectively, terminal voltage and current at the ac side. v_a is the sum of SM capacitor voltages in phase a upper arm. m_a and i_a are, respectively, insertion index and current of phase a upper arm, and $C = C_{\mathrm{m}}/N$ is the equivalent SM capacitance of each arm.

Similar to three-phase MMC, a series of harmonics are generated due to the complex couplings of electrical variables in SMs. The difference is that since there is no concept of phase sequence in single-phase MMC, all odd harmonics are DM components and flow into the ac side, while all even harmonics are CM components and flow into the dc side.

In a three-phase three-wire MMC system, since third harmonic currents are DM zero sequence and their amplitudes are zero, accurate ac or dc side second-order impedance models of a three-phase MMC could be obtained by only considering all electrical quantities within the third order. The obtained impedance matrix consists of positive and negative sequences and coupling components. While in single-phase MMC, the

amplitudes of third-order current harmonics are not zero and they flow into the ac side, which indicates that when establishing the admittance model of single-phase MMC, it is necessary to consider the influence of the fourth harmonics to achieve sufficient accuracy.

Therefore, the following modeling considers all variables within the fourth order. Complex vectors of variables in (1) can be expressed as (2) shown at the bottom of the this page

Take $\boldsymbol{m}_a$ as an example. M_{ak} ($k = 0, 1, 2, 3, 4$) and $\beta_{\rm k}$ are the amplitude and phase of the kth-order harmonic component of $m_{\rm a}$, respectively. Other symbols have similar meanings and, thus, are not repeated here.

Hence, the time-domain steady-state model (1) can be transformed into the frequency domain and written as

$$\begin{cases} 2\boldsymbol{Z}_{l0}\boldsymbol{i}_a = \boldsymbol{v}_{\rm dc} - 2\boldsymbol{m}_a \otimes \boldsymbol{v}_a - \boldsymbol{v}_{\rm ac} \\ \boldsymbol{Y}_{c0}\boldsymbol{v}_a = \boldsymbol{m}_a \otimes \boldsymbol{i}_a \end{cases} \tag{3}$$

where $\otimes$ is the symbol of convolution. $\boldsymbol{Z}_{l0}$ is a diagonal matrix representing the sum of arm inductance and equivalent ac impedance. $\boldsymbol{Y}_{c0}$ is the admittance of the equivalent SM capacitor. They are, respectively, expressed as

$$\begin{aligned} \mathbf{Z}_{l0} = {} & j2\pi L \cdot diag\left[-4f_1 \quad -3f_1 \quad -2f_1 \quad -f_1 \right. \\ & \left. 0 \quad f_1 \quad 2f_1 \quad 3f_1 \quad 4f_1 \right] \\ & + j4\pi L_m \\ & \times diag\left[0 \quad -3f_1 \quad 0 \quad -f_1 \quad 0 \quad f_1 \quad 0 \quad 3f_1 \quad 0 \right] \\ & +2 \cdot diag\left[r_{\rm m} \quad 0 \quad r_{\rm m} \quad 0 \quad r_{\rm m} \quad 0 \quad r_{\rm m} \quad 0 \quad r_{\rm m} \right] \end{aligned} \tag{4}$$

$$\begin{aligned} \boldsymbol{Y}_{c0} = {} & j2\pi C \cdot diag\left[-4f_1 \quad -3f_1 \quad -2f_1 \quad -f_1 \right. \\ & \left. 0 \quad f_1 \quad 2f_1 \quad 3f_1 \quad 4f_1 \right]. \end{aligned} \tag{5}$$

To obtain the ac admittance model, a sinusoidal voltage perturbation $\hat{v}_p$ with frequency $f_{\rm p}$ is added at the ac side. Then, a current response $\hat{i}_p$ with the perturbation frequency is generated. In addition, current responses with frequency $f_{\rm p}\pm 2kf_1$ (k is an integer) are also generated due to frequency coupling effects. These small-signal currents will generate new voltage perturbations across grid impedance and cause current responses circularly, which is also called the grid impedance coupling effect. To derive an accurate admittance model, three voltage perturbations with the frequencies of $f_{\rm p}$-$2f_1$, $f_{\rm p}$, and $f_{\rm p}$+$2f_1$ are added at the ac side.

According to the frequency-domain model (3), couplings between steady-state and small-signal components generate a series of small-signal harmonics with the frequency of $f_{\rm p}\pm kf_1$, where k is an integer. And these small signals satisfy the following rules:

$$f = \begin{cases} f_p + 2kf_1 & \text{differential mode} \\ f_p + (2k+1)f_1 & \text{common mode} \end{cases}. \tag{6}$$

After the linearization process of the steady-state model and to facilitate the operation, the convolution operations in the frequency-domain model are transformed into dot product operations. Thus, the small-signal model of the power stage of single-phase MMC-RPC can be derived as

$$\begin{cases} 2\boldsymbol{Z}_{l0}\hat{\boldsymbol{i}}_a = \hat{\boldsymbol{v}}_{\rm dc} - 2\boldsymbol{M}_a\hat{\boldsymbol{v}}_a - 2\boldsymbol{V}_a\hat{\boldsymbol{m}}_a - \hat{\boldsymbol{v}}_{\rm ac} \\ \boldsymbol{Y}_{c0}\hat{\boldsymbol{v}}_a = \boldsymbol{M}_a\hat{\boldsymbol{i}}_a + \boldsymbol{I}_a\hat{\boldsymbol{m}}_a \end{cases} \tag{7}$$

where $\boldsymbol{M}_a$, $\boldsymbol{V}_a$, and $\boldsymbol{I}_a$ are Toeplitz matrices of steady-state electrical variables and have similar forms, expressed as (8) shown at the bottom of the next page in a unified format.

B. Small-Signal Modeling of Control System and Third-Order AC Admittance of Single-Phase MMC-RPC

As shown in Fig. 3(a), the control system is constructed in the *dq* reference frame. Ac voltages and currents are transformed to the $\alpha\beta$ reference frame through the second-order generalized integrator (SOGI), as shown in Fig. 3(b), and then are transformed to the *dq* reference frame. Finally, the insertion index is obtained after passing through regulators of outer and inner control loops. As shown in Fig. 3(c), the phase-locked loop (PLL) adopts the SOGI-based single synchronous reference frame software structure, which is commonly used in single-phase systems. The small-signal model of the control system is the superposition of all control loops and can be modeled by

$$\begin{aligned} \hat{\boldsymbol{m}}_a = {} & (\boldsymbol{Q}_{i1} + \boldsymbol{Q}_{i2} + \boldsymbol{Q}_{i3} - \boldsymbol{Q}_v \cdot 2\boldsymbol{Z}_a + \boldsymbol{Q}_{qi})\hat{\boldsymbol{i}}_a \\ & + (\boldsymbol{Q}_{\rm pll} + \boldsymbol{Q}_{\rm feed} + \boldsymbol{Q}_{qv})\hat{\boldsymbol{v}}_{\rm ac} \end{aligned} \tag{9}$$

where $\boldsymbol{Q}_{i1}$, $\boldsymbol{Q}_{i2}$, and $\boldsymbol{Q}_{i3}$ are the coefficient matrices of the fundamental current control loop, second-harmonic circulating current suppressing control loop (CCSC), and third-harmonic current suppressing control loop (TCSC). $\boldsymbol{Q}_v$, $\boldsymbol{Q}_{\rm pll}$, and $\boldsymbol{Q}_{\rm feed}$ are, respectively, coefficient matrices of the dc voltage control loop, PLL, and feedforward control loop. $\boldsymbol{Q}_{qv}$ and $\boldsymbol{Q}_{qi}$ are coefficient matrices of the reactive power control loop. The effects of time delay are included in the above-mentioned coefficient matrices. As mentioned before, since the fourth harmonic component is considered in this article, the above-mentioned coefficient matrices are all nine-order square matrices, and the

$$\begin{cases} \boldsymbol{v}_{\rm dc} = \begin{bmatrix} 0 & 0 & 0 & 0 & U_{\rm dc} & 0 & 0 & 0 & 0 \end{bmatrix}^T \\ \boldsymbol{v}_{\rm ac} = \begin{bmatrix} 0 & 0 & 0 & 0.5V_1e^{-j\varphi_v} & 0 & 0.5V_1e^{j\varphi_v} & 0 & 0 & 0 \end{bmatrix}^T \\ \boldsymbol{i}_a = \begin{bmatrix} 0 & 0 & 0 & 0.5I_{a1}e^{-j\alpha_1} & I_{a0} & 0.5I_{a1}e^{j\alpha_1} & 0 & 0 & 0 \end{bmatrix}^T \\ \boldsymbol{m}_a = \begin{bmatrix} 0.5M_{a4}e^{-j\beta_4} & 0.5M_{a3}e^{-j\beta_3} & 0.5M_{a2}e^{-j\beta_2} & 0.5M_{a1}e^{-j\beta_1} \\ M_{a0} & 0.5M_{a1}e^{j\beta_1} & 0.5M_{a2}e^{j\beta_2} & 0.5M_{a3}e^{j\beta_3} & 0.5M_{a4}e^{j\beta_4} \end{bmatrix}^T \\ \boldsymbol{v}_a = \begin{bmatrix} 0.5V_{a4}e^{-j\gamma_4} & 0.5V_{a3}e^{-j\gamma_3} & 0.5V_{a2}e^{-j\gamma_2} & 0.5V_{a1}e^{-j\gamma_1} \\ V_{a0} & 0.5V_{a1}e^{j\gamma_1} & 0.5V_{a2}e^{j\gamma_2} & 0.5V_{a3}e^{j\gamma_3} & 0.5V_{a4}e^{j\gamma_4} \end{bmatrix}^T. \end{cases} \tag{2}$$

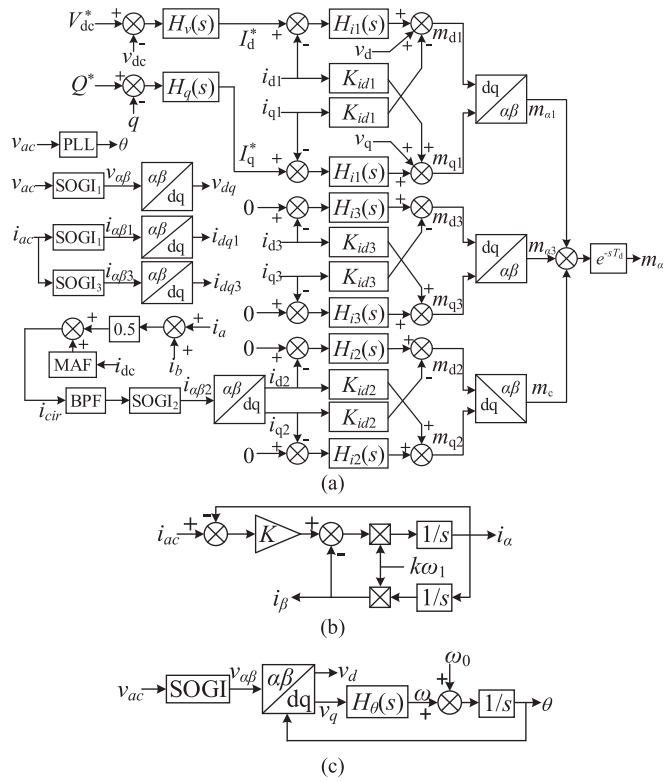

Fig. 3. Control block diagrams of (a) single-phase MMC-RPC, (b) SOGI, and (c) PLL.

element parameters in these matrices are related to the structure and parameters of the control loops.

1) Fundamental Current Control, CCSC, and TCSC: The fundamental current control mainly regulates currents flowing into the ac side. According to (6), this control loop works on small-signal harmonics with the frequency of $f_p \pm 2kf_1$ ($k = 0, 1, 2$). Hence, the coefficient matrix is represented as

$$\boldsymbol{Q}_{i1} = diag\begin{bmatrix} a_{-4} & 0 & a_{-2} & 0 & a_0 & 0 & a_2 & 0 & a_4 \end{bmatrix}. \quad (10)$$

The small-signal current harmonics go through SOGI and Park transformation, and then the frequencies of these currents are shifted upward and down by f_1 due to the asymmetry in the $\alpha\beta$ reference frame. This asymmetry also complicates the frequency coupling effects in the admittance model. And then the small-signal insertion index could be obtained through PI controllers and inverse Park transformation. The elements in $\boldsymbol{Q}_{i1}$ could be expressed as

$$\begin{aligned} a_k = \frac{1}{2}[&(H_i(j2\pi(f_p + (k-1)\cdot f_1)) \\ &+ H_i(j2\pi(f_p + (k+1)\cdot f_1)))H_\alpha(f_p + k\cdot f_p) \\ &+ (jH_i(j2\pi(f_p + (k-1)\cdot f_1)) + 2K_{id} \\ &- jH_i(j2\pi(f_p + (k+1)\cdot f_1)))H_\beta(f_p + k\cdot f_p)]G_{Tdk} \end{aligned} \quad (11)$$

where $G_{Tdk} = \mathrm{e}^{-j2\pi(f_\mathrm{p}+kf_1)T_\mathrm{d}}$, and $k = -4, -2, 0, 2, 4$.

Similarly, CCSC and TCSC work on the harmonic currents with the frequency of $f_\mathrm{p} \pm (2k+1)f_1$ ($k = 0, 1$) and $f_\mathrm{p} \pm 2kf_1$ ($k = 0, 1, 2$), respectively. Thus the coefficient matrices of these two control loops are

$$\boldsymbol{Q}_{i2} = diag\begin{bmatrix} 0 & b_{-3} & 0 & b_{-1} & 0 & b_1 & 0 & b_3 & 0 \end{bmatrix} \quad (12)$$

$$\boldsymbol{Q}_{i3} = diag\begin{bmatrix} c_{-4} & 0 & c_{-2} & 0 & c_0 & 0 & c_2 & 0 & c_4 \end{bmatrix} \quad (13)$$

where

$$\begin{aligned} b_k = \frac{1}{2}((&H_i(j2\pi(f_p + (k-2)\cdot f_1)) \\ &+ H_i(j2\pi(f_p + (k+2)\cdot f_1)))H_{\alpha 2}(f_p + k\cdot f_1) \\ &\times H_{bpf}(j2\pi(f_p + k\cdot f_1)) + (jH_i(j2\pi(f_p + (k-2)\cdot f_1)) \\ &- 2K_\mathrm{id} - jH_i(j2\pi(f_p + (k+2)\cdot f_1))) \\ &\times H_{\beta 2}(f_p + k\cdot f_1)H_{bpf}(j2\pi(f_p + k\cdot f_1)))G_{Tdk} \end{aligned}$$
$$(k = -3, -1, 1, 3) \quad (14)$$

$$\begin{aligned} c_k = \frac{1}{2}[&(H_i(j2\pi(f_p + (k-3)\cdot f_1)) \\ &+ H_i(j2\pi(f_p + (k+3)\cdot f_1)))H_{\alpha 3}(f_p + k\cdot f_p) \\ &+ (jH_i(j2\pi(f_p + (k-3)\cdot f_1)) + 2K_{id} \\ &- jH_i(j2\pi(f_p + (k+3)\cdot f_1)))H_{\beta 3}(f_p + k\cdot f_p)]G_{Tdk} \end{aligned}$$
$$(k = -4, -2, 0, 2, 4). \quad (15)$$

It is found that the initial phase of grid voltage φ_v does not influence the modeling of these three current control loops.

2) DC Voltage Control: Harmonic components with the frequency of $f_\mathrm{p} \pm (2k+1)f_1$ ($k = 0, 1$) in dc voltage are successively regulated by the dc voltage controller, the fundamental current controller, and the inverse Park transformation to obtain the small-signal insertion index. The coefficient matrix of dc voltage

$$\boldsymbol{X} = \frac{1}{2}\begin{bmatrix} 2X_0 & X_1e^{-j\delta_1} & X_2e^{-j\delta_2} & X_3e^{-j\delta_3} & 0 & 0 & 0 \\ X_1e^{j\delta_1} & 2X_0 & X_1e^{-j\delta_1} & X_2e^{-j\delta_2} & X_3e^{-j\delta_3} & 0 & 0 \\ X_2e^{j\delta_2} & X_1e^{j\delta_1} & 2X_0 & X_1e^{-j\delta_1} & X_2e^{-j\delta_2} & X_3e^{-j\delta_3} & 0 \\ X_3e^{j\delta_3} & X_2e^{j\delta_2} & X_1e^{j\delta_1} & 2X_0 & X_1e^{-j\delta_1} & X_2e^{-j\delta_2} & X_3e^{-j\delta_3} \\ 0 & X_3e^{j\delta_3} & X_2e^{j\delta_2} & X_1e^{j\delta_1} & 2X_0 & X_1e^{-j\delta_1} & X_2e^{-j\delta_2} \\ 0 & 0 & X_3e^{j\delta_3} & X_2e^{j\delta_2} & X_1e^{j\delta_1} & 2X_0 & X_1e^{-j\delta_1} \\ 0 & 0 & 0 & X_3e^{j\delta_3} & X_2e^{j\delta_2} & X_1e^{j\delta_1} & 2X_0 \end{bmatrix}$$
$$(\boldsymbol{X} = \boldsymbol{M}_a, \boldsymbol{V}_a, \boldsymbol{I}_a). \quad (8)$$

control can be represented as (16) shown at the bottom of the this page

The dc voltage harmonics are regulated by the dc voltage controller and fundamental current controller and then added to the insertion index after inverse Park transformation. The frequencies of these harmonics are also shifted upward and down by f_1 due to the asymmetry in the dq reference frame. After derivation, the elements in $\boldsymbol{Q}_v$ could be expressed as (17). It is also found that the initial phase of grid voltage has effects on the modeling of dc voltage control, which is always ignored in other papers.

$$m_k = -\frac{1}{4}H_v(j2\pi(f_p + kf_1))H_i(j2\pi(f_p + kf_1)) \tag{17}$$

where $k = -3, -1, 0, 1, 3$.

3) Feedforward Control: Ac voltage harmonics with the frequency of $f_p \pm 2kf_1$ ($k = 0, 1, 2$) are fed directly to the insertion index after passing through SOGI and the Park transformation. The coefficient matrix is expressed as

$$\boldsymbol{Q}_{\text{feed}} = diag\begin{bmatrix} n_{-4} & 0 & n_{-2} & 0 & n_0 & 0 & n_2 & 0 & n_4 \end{bmatrix} \tag{18}$$

where

$$n_k = 0.5H_\alpha(j2\pi(f_p + kf_1))G_{Tdk}, (k = -4, -2, 0, 2, 4). \tag{19}$$

4) Reactive Power Control: The steady-state reactive power compensated to the traction power grid is

$$q = 1.5(v_q i_d - v_d i_q). \tag{20}$$

The q-axis steady-state component of ac voltage is zero. Thus, small-signal reactive power could be simplified as

$$\hat{q} = 1.5(I_d\hat{v}_q - V_d\hat{i}_q - I_q\hat{v}_d) \tag{21}$$

which includes three terms. Thus, the coefficient matrix of reactive power control is the superposition of these three terms. As in previous control loops, coefficient matrices $\boldsymbol{Q}_{qv}$ and $\boldsymbol{Q}_{qi}$ can be calculated. Detailed expressions of $\boldsymbol{Q}_{qv}$ and $\boldsymbol{Q}_{qi}$ are not shown here due to space limitations.

5) Phase-Locked Loop: Small-signal ac voltage harmonics cause disturbances in the phases locked by PLL, which influence all segments containing Park transformation and inverse Park transformation. Here take the ac voltage harmonic with the frequency of f_p as an example to derive the small-signal harmonics in the output phase of PLL. Assume the ac voltage is

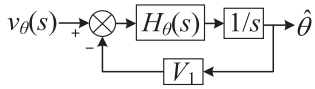

Fig. 4. Block diagram of the linearized model of PLL.

expressed as

$$v_{\text{ac}} = V_1\cos(\theta_1 + \varphi_v) + V_p\cos(2\pi f_p t + \varphi_p). \tag{22}$$

After passing through SOGI, ac voltage components in the $\alpha\beta$ reference frame are represented as

$$\begin{bmatrix} V_\alpha \\ V_\beta \end{bmatrix} = \begin{bmatrix} V_1\cos(\theta_1 + \varphi_v) + V_\alpha\cos(\theta_p + \varphi_\alpha) \\ V_1 sin(\theta_1 + \varphi_v) + V_\beta\cos(\theta_p + \varphi_\beta) \end{bmatrix} \tag{23}$$

where

$$\begin{cases} V_\alpha e^{j\varphi_\alpha} = H_\alpha(j2\pi f_p)V_s e^{j\varphi_p} \\ V_\beta e^{j\varphi_\beta} = H_\beta(j2\pi f_p)V_s e^{j\varphi_p}. \end{cases} \tag{24}$$

After passing through the Park transformation in which the phases contain harmonics, ac voltage in the q-axis is obtained

$$\begin{aligned} v_q \approx & -V_1\hat{\theta} - \frac{V_\alpha}{2}(\sin(\theta_p + \theta_1 + \varphi_\alpha + \varphi_v) \\ & - \sin(\theta_p - \theta_1 + \varphi_\alpha - \varphi_v)) + \frac{V_\beta}{2} \\ & \times(\cos(\theta_p + \theta_1 + \varphi_\beta + \varphi_v) + \cos(\theta_p - \theta_1 + \varphi_\beta - \varphi_v)). \end{aligned} \tag{25}$$

The equivalent diagram of PLL is shown in Fig. 4, where

$$\begin{aligned} v_\theta = & -\frac{V_\alpha}{2}(\sin(\theta_p + \theta_1 + \varphi_\alpha + \varphi_v) \\ & - \sin(\theta_p - \theta_1 + \varphi_\alpha - \varphi_v)) \\ & + \frac{V_\beta}{2}(\cos(\theta_p + \theta_1 + \varphi_\beta + \varphi_v) \\ & + \cos(\theta_p - \theta_1 + \varphi_\beta - \varphi_v)). \end{aligned} \tag{26}$$

Hence, the closed-loop transfer function of PLL is

$$G_\theta(s) = \frac{H_\theta(s)/s}{1 + V_1 H_\theta(s)/s}. \tag{27}$$

The small-signal harmonics of the output phase can be expressed as

$$\hat{\theta} = G_\theta(s) \cdot v_\theta. \tag{28}$$

$$\boldsymbol{Q}_v = \begin{bmatrix} 0 & m_{-3}e^{-j\varphi_v}G_{Td-4} & 0 & 0 & 0 & 0 & 0 & 0 & 0 \\ 0 & 0 & 0 & 0 & 0 & 0 & 0 & 0 & 0 \\ 0 & m_{-3}e^{j\varphi_v}G_{Td-2} & 0 & m_{-1}e^{-j\varphi_v}G_{Td-2} & 0 & 0 & 0 & 0 & 0 \\ 0 & 0 & 0 & 0 & 0 & 0 & 0 & 0 & 0 \\ 0 & 0 & 0 & m_{-1}e^{j\varphi_v}G_{Td0} & 0 & m_1e^{-j\varphi_v}G_{Td0} & 0 & 0 & 0 \\ 0 & 0 & 0 & 0 & 0 & 0 & 0 & 0 & 0 \\ 0 & 0 & 0 & 0 & 0 & m_1e^{j\varphi_v}G_{Td2} & 0 & m_3e^{-j\varphi_v}G_{Td2} & 0 \\ 0 & 0 & 0 & 0 & 0 & 0 & 0 & 0 & 0 \\ 0 & 0 & 0 & 0 & 0 & 0 & 0 & m_3e^{-j\varphi_v}G_{Td4} & 0 \end{bmatrix}. \tag{16}$$

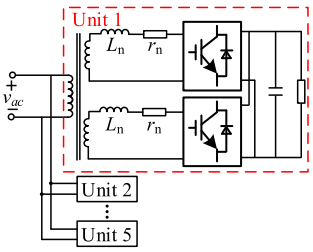

Fig. 5. Block diagram of the rectifiers in one vehicle.

It can be found that the small-signal voltage harmonic with the frequency of f_p can generate harmonics with the frequency of f_p+f_1 and f_p-f_1 in the output phases, which is related to the initial phase of the grid voltage. This is very different from that in three-phase MMC and is also caused by the asymmetry brought by SOGI. Similarly, ac voltage harmonics with the frequency of $f_p \pm 2f_1$ and $f_p \pm 4f_1$ also generate small-signal disturbances in the output phase of PLL. According to these phase disturbances, the model of PLL can be established. The rest of the derivations are similar to that in three-phase MMC and thus are not expanded in detail here. It can be observed in (26) and (28) that the initial phase of grid voltage has non-negligible effects on the modeling of PLL.

6) AC Admittance Model of Single-Phase MMC-RPC: Finally, combining the small-signal models of the power stage and control system, the relationship between the small-signal response of the ac side current and the ac voltage perturbation is

$$\boldsymbol{Y}_{ac}=(\boldsymbol{Z}_{l0}+\boldsymbol{Z}_a+\boldsymbol{M}_a\boldsymbol{Z}_{c0}\boldsymbol{M}_a+(\boldsymbol{M}_a\boldsymbol{Z}_{c0}\boldsymbol{I}_a+\boldsymbol{V}_a)\boldsymbol{P}_i)^{-1} \cdot(\boldsymbol{U}+2(\boldsymbol{M}_a\boldsymbol{Z}_{c0}\boldsymbol{I}_a+\boldsymbol{V}_a)\boldsymbol{P}_v) \tag{29}$$

where $\boldsymbol{U}$ is the identity matrix. $\boldsymbol{Z}_{c0}=\boldsymbol{Y}_{c0}^{-1}$

$$\begin{aligned}\boldsymbol{P}_i &= \boldsymbol{Q}_{i1}+\boldsymbol{Q}_{i3}+\boldsymbol{Q}_c-\boldsymbol{Q}_v\cdot 2\boldsymbol{Z}_a+\boldsymbol{Q}_{qi}\\ \boldsymbol{P}_v &= \boldsymbol{Q}_{\text{pll}}+\boldsymbol{Q}_{\text{feed}}+\boldsymbol{Q}_{qv}.\end{aligned} \tag{30}$$

Hence, the third-order ac admittance model of single-phase MMC-RPC is expressed as

$$\boldsymbol{Y}_{\text{MMC-RPC}}=\begin{bmatrix}\boldsymbol{Y}_{\text{ac}}(3,3) & \boldsymbol{Y}_{\text{ac}}(3,5) & \boldsymbol{Y}_{\text{ac}}(3,7)\\ \boldsymbol{Y}_{\text{ac}}(5,3) & \boldsymbol{Y}_{\text{ac}}(5,5) & \boldsymbol{Y}_{\text{ac}}(5,7)\\ \boldsymbol{Y}_{\text{ac}}(7,3) & \boldsymbol{Y}_{\text{ac}}(7,5) & \boldsymbol{Y}_{\text{ac}}(7,7)\end{bmatrix}. \tag{31}$$

III. AC Admittance Modeling of Vehicle Rectifiers

As shown in Fig. 5, each vehicle contains five motive units and each unit has dual single-phase interleaved converters sharing one common dc-link capacitor. Each unit can be equalized as two independent rectifiers due to their identical controllers and circuits [17]. Thus, every vehicle has ten paralleled rectifiers. To simplify the analysis, the dc-link load could be equivalent to a resistor [19]. This section will first establish the ac admittance model of a single rectifier, and according to the connection relations of multiple units, the ac admittance model of the whole vehicle can be obtained.

A. Steady-State and Small-Signal Modeling of Power Stage

Existing literature has proved that it is sufficient to obtain accurate impedance models of single-phase two-level converters when considering harmonics within the fourth order [23]. But they only took the middle element in the matrix as the SISO impedance or only considered the second-order impedance matrix at f_p and f_p-$2f_1$. Consistent with single-phase MMC-RPC, the third-order ac admittance model of the vehicle rectifier will be developed here, considering the fourth and lower harmonics of variables. According to the main circuit of the vehicle rectifier, the time-domain steady-state averaged model of the power stage is represented as

$$\begin{cases}L_n\dfrac{di_s}{dt}+r_n i_s=v_{ac}-mv_{dc}\\ C_d\dfrac{dv_{dc}}{dt}+\dfrac{1}{R_d}v_{dc}=mi_s\end{cases} \tag{32}$$

where v_{ac} and i_s are, respectively, the ac voltage and ac current. v_{dc} is the dc voltage, and m is the insertion index. L_n and r_n are the equivalent inductance and resistance of the traction transformer. C_d is the dc-link capacitance.

The time-domain averaged model could be transformed to the frequency domain similarly and expressed as

$$\begin{cases}\boldsymbol{Z}_n\boldsymbol{i}_s=\boldsymbol{v}_{ac}-\boldsymbol{m}\otimes\boldsymbol{v}_{dc}\\ \boldsymbol{Y}_{dc}\boldsymbol{v}_{dc}=\boldsymbol{m}\otimes\boldsymbol{i}_s.\end{cases} \tag{33}$$

$\boldsymbol{Z}_n$ and $\boldsymbol{Y}_{dc}$ are separately the equivalent impedance of the ac transformer and the equivalent admittance of dc load, which can be expressed in a similar format, as shown in (4) and (5). Other electrical variables in (33) are all nine-dimensional column vectors.

The harmonic characteristics are similar to that in single-phase MMC-RPC. Therefore, according to the principle of the multi-harmonic linearization method, voltage perturbations at f_p-$2f_1$, f_p, and f_p+$2f_1$ are added at the ac side.

After the linearization process and transforming the convolution operation to dot product operation, the frequency-domain model of the power stage can be represented as

$$\begin{cases}\boldsymbol{Z}_n\hat{\boldsymbol{i}}_s=\hat{\boldsymbol{v}}_{ac}-\boldsymbol{M}\hat{\boldsymbol{v}}_{dc}-\boldsymbol{V}_{dc}\hat{\boldsymbol{m}}\\ \boldsymbol{Y}_{dc}\hat{\boldsymbol{v}}_{dc}=\boldsymbol{M}\hat{\boldsymbol{i}}_s+\boldsymbol{I}_s\hat{\boldsymbol{m}}\end{cases} \tag{34}$$

where $\boldsymbol{M}$, $\boldsymbol{V}_{dc}$, and $\boldsymbol{I}_s$ are, respectively, the Toeplitz forms of insertion index, dc voltage, and ac current, which could also be represented as the unified format in (8).

B. Small-Signal Modeling of Control System and Third-Order AC Admittance of Vehicle Rectifiers

As shown in Fig. 6, the control system is also based on the *dq* reference frame. The PLL adopts the SOGI-based single synchronous reference frame software structure. The small-signal model of the control system is the superposition of all control loops and is represented as

$$\hat{\boldsymbol{m}}=\boldsymbol{Q}_{vdc}\hat{\boldsymbol{v}}_{dc}+\boldsymbol{Q}_i\hat{\boldsymbol{i}}_s+(\boldsymbol{Q}_{\text{feed}}+\boldsymbol{Q}_{\text{pll}})\hat{\boldsymbol{v}}_p \tag{35}$$

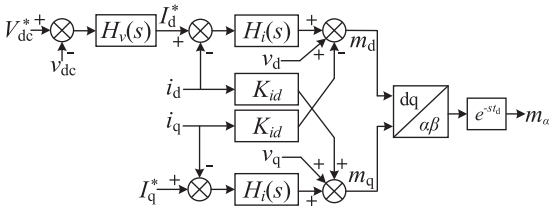

Fig. 6. Block diagram of the control system of the vehicle rectifier.

where $\boldsymbol{Q}_{vdc}$, $\boldsymbol{Q}_i$, $\boldsymbol{Q}_{\text{feed}}$, and $\boldsymbol{Q}_{\text{pll}}$ are, respectively, the coefficient matrices of the dc voltage control, phase current control, feedforward control, and PLL, which are also of the nine order. The effects of time delay are included in the abovementioned four coefficient matrices.

1) Phase Current Control: Like the single-phase MMC-RPC, phase current control in the vehicle rectifier works on the current harmonics with the frequency of $f_p \pm 2kf_1$ ($k = 0, 1, 2$). Thus, the coefficient matrix of this control loop could be written as

$$\boldsymbol{Q}_i = diag\begin{bmatrix} a_{-4} & 0 & a_{-2} & 0 & a_0 & 0 & a_2 & 0 & a_4 \end{bmatrix} \quad (36)$$

where

$$\begin{aligned} a_k = \frac{1}{2}[&(H_i(j2\pi(f_p + (k-1)f_1)) \\ &+ H_i(j2\pi(f_p + (k+1)f_1)))H_\alpha(f_p + kf_p) \\ &+ (jH_i(j2\pi(f_p + (k-1)f_1)) + 2K_{id} \\ &- jH_i(j2\pi(f_p + (k+1)f_1)))H_\beta(f_p + kf_p)]G_{tdk} \\ &(k = -4, -2, 0, 2, 4) \end{aligned} \quad (37)$$

where $G_{tdk} = \mathrm{e}^{-j2\pi(f_p + kf_1)t_d}$.

2) DC Voltage Control: Dc voltage control loop works on the dc voltage harmonics with the frequency of $f_p \pm (2k+1)f_1$ ($k = 0, 1$). The detailed derivation process is similar to that in the single-phase MMC-RPC, thus, the coefficient matrix is directly written as (38) shown at the bottom of the this page where

$$\begin{aligned} m_k = &\frac{1}{2}H_v(j2\pi(f_p + kf_1))H_i(j2\pi(f_p + kf_1)) \\ &(k = -3, -1, 1, 3). \end{aligned} \quad (39)$$

3) Feedforward Control: Similar to the feedforward control in single-phase and three-phase MMC, the ac voltage is directly fed to the insertion index, thus, the coefficient matrix could be written as

$$\boldsymbol{Q}_{\text{feed}} = diag\begin{bmatrix} n_{-4} & 0 & n_{-2} & 0 & n_0 & 0 & n_2 & 0 & n_4 \end{bmatrix} \quad (40)$$

where

$$n_k = H_\alpha(j2\pi(f_p + k \cdot f_1))G_{tdk}, (k = -4, -2, 0, 2, 4). \quad (41)$$

4) Phase-Locked Loop: Small-signal ac voltage harmonics will cause disturbances in the output phase of PLL and influence all segments containing Park transformation and inverse Park transformation. The detailed derivations of PLL are similar to that in single-phase MMC-RPC, thus, are not repeated here.

5) AC Admittance Model of Vehicle Rectifiers: Combining the small-signal models of the power stage and control system, the relationship between the small-signal response of the ac current and the ac voltage perturbation is

$$\begin{aligned} \boldsymbol{Y}_{\text{ac}} = &(\boldsymbol{Z}_l + \boldsymbol{V}_{\text{dc}}\boldsymbol{Q}_i + (\boldsymbol{M} + \boldsymbol{V}_{\text{dc}}\boldsymbol{Q}_{vdc}) \cdot (\boldsymbol{Y}_{\text{dc}} - \boldsymbol{I}_s\boldsymbol{Q}_{vdc})^{-1} \\ &\cdot (\boldsymbol{M} + \boldsymbol{I}_s\boldsymbol{Q}_i))^{-1} \cdot (\boldsymbol{U} - \boldsymbol{V}_{\text{dc}}\boldsymbol{Q}_{vac} - (\boldsymbol{M} + \boldsymbol{V}_{\text{dc}}\boldsymbol{Q}_{vdc}) \\ &\cdot (\boldsymbol{Y}_{\text{dc}} - \boldsymbol{I}_s\boldsymbol{Q}_{vdc})^{-1}\boldsymbol{I}_s\boldsymbol{Q}_{vac}) \end{aligned} \quad (42)$$

where $\boldsymbol{U}$ is the identity matrix. $\boldsymbol{Z}_{\text{dc}} = \boldsymbol{Y}_{\text{dc}}^{-1}$. $\boldsymbol{Q}_{vac} = \boldsymbol{Q}_{\text{feed}} + \boldsymbol{Q}_{\text{pll}}$.

The ac admittance of each vehicle is

$$\boldsymbol{Y}_{\text{AC}} = n \cdot \boldsymbol{Y}_{\text{ac}}/k^2 \quad (43)$$

where k is the ratio of the high voltage side to the low voltage side of the transformer. n is the number of rectifiers in each vehicle, and here n equals 10.

Hence, the equivalent third-order ac admittance of one vehicle is represented as

$$\boldsymbol{Y}_{vsc} = \begin{bmatrix} \boldsymbol{Y}_{\text{AC}}(3,3) & \boldsymbol{Y}_{\text{AC}}(3,5) & \boldsymbol{Y}_{\text{AC}}(3,7) \\ \boldsymbol{Y}_{\text{AC}}(5,3) & \boldsymbol{Y}_{\text{AC}}(5,5) & \boldsymbol{Y}_{\text{AC}}(5,7) \\ \boldsymbol{Y}_{\text{AC}}(7,3) & \boldsymbol{Y}_{\text{AC}}(7,5) & \boldsymbol{Y}_{\text{AC}}(7,7) \end{bmatrix}. \quad (44)$$

C. Verification of the Proposed AC Admittance Models

To verify the correctness and accuracy of the admittance models proposed in Sections II and III, detailed time-domain simulation models of the single-phase MMC-RPC and the vehicle rectifier are separately established in MATLAB/ Simulink.

$$\boldsymbol{Q}_{vdc} = \begin{bmatrix} 0 & m_{-3}e^{-j\varphi_v}G_{td-4} & 0 & 0 & 0 & 0 & 0 & 0 & 0 \\ 0 & 0 & 0 & 0 & 0 & 0 & 0 & 0 & 0 \\ 0 & m_{-3}e^{j\varphi_v}G_{td-2} & 0 & m_{-1}e^{-j\varphi_v}G_{td-2} & 0 & 0 & 0 & 0 & 0 \\ 0 & 0 & 0 & 0 & 0 & 0 & 0 & 0 & 0 \\ 0 & 0 & 0 & m_{-1}e^{j\varphi_v}G_{td0} & 0 & m_1e^{-j\varphi_v}G_{td0} & 0 & 0 & 0 \\ 0 & 0 & 0 & 0 & 0 & 0 & 0 & 0 & 0 \\ 0 & 0 & 0 & 0 & 0 & m_1e^{j\varphi_v}G_{td2} & 0 & m_3e^{-j\varphi_v}G_{td2} & 0 \\ 0 & 0 & 0 & 0 & 0 & 0 & 0 & 0 & 0 \\ 0 & 0 & 0 & 0 & 0 & 0 & 0 & m_3e^{-j\varphi_v}G_{td4} & 0 \end{bmatrix} \quad (38)$$

TABLE I
ELECTRICAL PARAMETERS OF SINGLE-PHASE MMC-RPC AND VEHICLE RECTIFIERS

Parameter	Symbol	Value
Single-phase MMC-RPC		
Rated ac voltage	V_{grms}	27.5 kV
Rated dc voltage	V_{dc}	50 kV
Rated power	P	30 MW
Fundamental frequency	f_1	50 Hz
SM capacitance	C_m	12 mF
Number of SM/arm	N	20
Arm inductance	L_0	10 mH
Equivalent series inductance	L_m	2 mH
Equivalent series resistance	R_m	0.2 Ω
Time delay	T_d	250 μs
Vehicle rectifier		
Rated ac voltage	V_{grms}	1.5 kV
Rated dc voltage	V_{dc}	3 kV
Rated power	P	0.36 MW
Transformer inductance	L_n	5.4 mH
Transformer resistance	R_n	0.2 Ω
DC-link capacitance	C_d	9 mF
DC-link resistance load	R_d	25 Ω
Time delay	t_d	150 μs

TABLE II
CONTROL PARAMETERS OF SINGLE-PHASE MMC-RPC AND VEHICLE RECTIFIERS

Parameter	Symbol	Value
Single-phase MMC-RPC		
DC voltage control	(K_{pU}, K_{iU})	(0.5, 100)
Reactive power control	(K_{pQ}, K_{iQ})	(3, 10)
Fundamental current control	(K_{pI1}, K_{iI1})	(0.2, 2.5)
CCSC	(K_{pI2}, K_{iI2})	(0.5, 20)
TCSC	(K_{pI3}, K_{iI3})	(0.1, 1)
PLL	(K_{pPLL}, K_{iPLL})	(180, 3200)
Feedforward control	K_F	1
Vehicle rectifier		
DC voltage control	(K_{pu}, K_{iu})	(2.5, 100)
Phase current control	(K_{pi}, K_{ii})	(2, 8)
PLL	(K_{ppll}, K_{ipll})	(180, 3200)
Feedforward control	K_f	1

Parameters of the power stage and control system of the single-phase MMC-RPC and the vehicle rectifier are listed in Tables I and II.

The frequency sweeping method is applied to get the admittance measurement results. It is demonstrated from the admittance curves, as shown in Fig. 7, that measurement and analysis results match well, verifying the accuracy of the proposed admittance models. It is also found that there are small errors between the measurement and analysis results in the high-frequency range of coupling admittances, which will not influence the LFO analysis of the single-phase MMC-RPC integrated vehicle-grid coupling system.

Admittance phases of the single-phase MMC-RPC, when the fourth harmonics or the effects of grid impedance coupling or the initial phase of the reference frame are ignored, are compared with the accurate model in Fig. 8. It is indicated from the comparison results that the fourth harmonics have non-negligible impacts on all coupled and uncoupled admittance elements in the full frequency range. The impacts are especially reflected in the diagonal elements near 100 Hz and are mainly determined by the arm inductance of single-phase MMC-RPC.

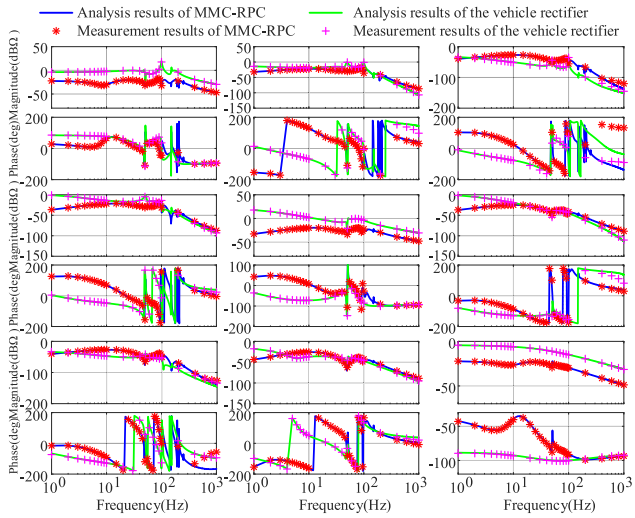

Fig. 7. Admittance response of single-phase MMC-RPC and single vehicle rectifier.

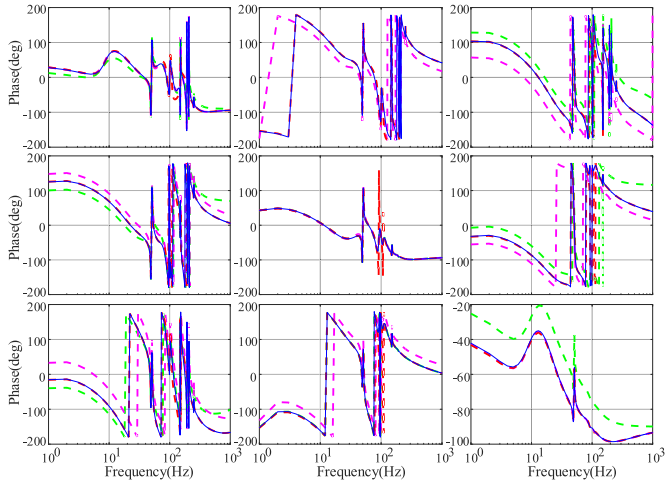

Fig. 8. Admittance phase response of the single-phase MMC-RPC with different accuracy: Accurate model (blue solid lines); Without considering the fourth harmonics (red dashed lines); Without considering the effects of the initial phase of the reference frame (pink dashed lines); Without considering grid impedance coupling effects (green dashed lines).

Because the arm inductance has a strong influence on the amplitudes of circulating currents in single-phase MMC-RPC, and the frequencies of the main circulating currents are exactly 100 Hz (the second harmonics) and 200 Hz (the fourth harmonics). The smaller the arm inductance, the more significant the influence of the fourth harmonics. The actual initial phase of the grid voltage is -12° instead of 0°. If the effects of the initial phase of the reference frame are ignored, the whole frequency range of the coupled admittances will be influenced, especially the low-frequency band, which will cause errors in the mechanism analysis of LFOs in the following sections. It is also observed that the whole frequency range of the first and third columns of the admittance matrix is greatly affected by the grid impedance coupling effects. Above all, the effects of frequency coupling, grid impedance coupling, and the initial phase of the reference

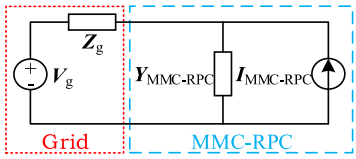

Fig. 9. Equivalent circuit of the interconnected system consisting of a single-phase MMC-RPC and traction power grid.

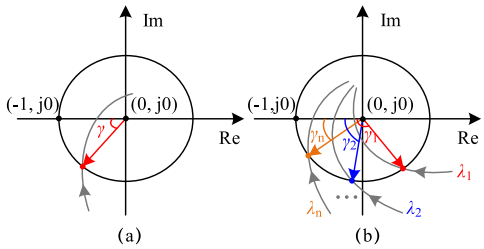

Fig. 10. Block diagram of (a) phase margin in SISO systems and (b) modal phase margin in MIMO systems.

frame are all non-negligible in the mechanism analysis of LFOs in the single-phase MMC-RPC integrated vehicle-grid coupling system.

IV. Mechanism Analysis of LFOs Caused by the Interactions of Single-Phase MMC-RPC and Traction Power Grid

Combined with the GNC, this section proposes a modal analysis method based on the indices of modal phase margin (MPM) and parameter sensitivity to evaluate the influence of parameters quantitatively. The impacts of parameters when varying in a wide range and an adjacent range could be comprehensively studied. Dominant modes, key parameters, and key control loops causing system instability can be clarified, and a series of guidelines can also be proposed for system stability enhancement. This section will focus on the interaction stability analysis between single-phase MMC-RPC and the power grid when there are no vehicle loads under the right feeder section, which means that MMC-RPC transmits active power to the left feeder section and compensates reactive power to the right side traction power grid.

A. Modal Analysis Method Combined with the GNC

According to the impedance-based stability analysis method, the equivalent circuit of the interconnected system consisting of a single-phase MMC-RPC and the power grid is shown in Fig. 9, where the power grid is equivalent to a voltage source subsystem with output impedance $\boldsymbol{Z}_{\rm g}$ and the MMC-RPC is equivalent to a current source subsystem with input admittance $\boldsymbol{Y}_{\rm MMC\text{-}RPC}$. Since the system is stable when single-phase MMC-RPC is connected to an ideal grid, $\boldsymbol{Y}_{\rm MMC\text{-}RPC}$ has no right-half-plane (RHP) poles. $\boldsymbol{Z}_{\rm g}$ is purely passive and, thus, also has no RHP poles. According to the GNC, the interconnected system is stable when the total number of counterclockwise encirclements of the critical point $(-1, {\rm j}0)$ by the eigen-loci of $\boldsymbol{Z}_{\rm g}\boldsymbol{Y}_{\rm MMC\text{-}RPC}$ equals zero.

For the SISO system, as shown in Fig. 10(a), phase margin γ is defined as the angle between $(-1, {\rm j}0)$ with the intersection point of the Nyquist curve of impedance ratio and unit circle relative to the original point (0, j0). Similarly, when applying GNC in MIMO systems, MPM is defined here. Assume the impedance ratio of one MIMO system has n eigenvalues, which are defined as n modes. Each Nyquist curve has one intersection point with the unit circle. As shown in Fig. 10(b), the MPM of each mode is defined as the angle between $(-1, {\rm j}0)$ with its intersection point relative to the original point (0, j0). The minimum of all MPMs is the system phase margin, and the corresponding eigenvalue is defined as the dominant mode. Besides, all the eigenvalues can be divided into three categories based on the value of MPM:

$$\lambda = \begin{cases} \text{strong–damping mode} & \text{MPM} > 60^{\rm o} \\ \text{weak–damping mode} & 0^{\rm o} \le \text{MPM} \le 60^{\rm o} \\ \text{unstable mode} & \text{MPM} < 0^{\rm o} \end{cases}. \quad (45)$$

To quantitatively compare the effects of different parameters on system stability, this article will first study the changing rules of the MPM of different eigenvalues with parameters varying in a wide range, which represents the global influence of parameters on system stability and the monotonicity of the influence and can identify the dominant mode. Then, this article will analyze parameter sensitivity with parameters varying in an adjacent range, which represents the local influence of the parameters and the participation degree of each parameter in the modal stability and can identify the key parameters. Finally, by combining the characteristic analysis of MPM and parameter sensitivity analysis, the dominant mode and key parameters of the studied MIMO system could be clarified, and parameter optimization guidelines could also be proposed. Therein, the sensitivity of parameter p on the MPM of eigenvalue λ_i is defined as

$$\begin{aligned} S_{\rm MPM}(p, f) &= \frac{\text{MPM}(\lambda_i(p')) - \text{MPM}(\lambda_i(p'_0))}{p' - p'_0} \\ &= \frac{\text{MPM}(\lambda_i(p'_0 + kp'_0)) - \text{MPM}(\lambda_i(p'_0))}{kp'_0} \end{aligned} \quad (46)$$

where $p' = p/p_0$. p_0 is the original parameter value, and k is the perturbation percentage of p_0. In general, the range of k is about 5%–10%.

B. Interaction Stability Analysis Between Single-Phase MMC-RPC and Traction Power Grid

Four working conditions are considered here to analyze the system stability comprehensively. 1) The compensated active power is 5 MW; 2) The compensated active power is 10 MW; 3) The compensated active power is 15 MW; 4) The compensated active power is 20 MW. Compensated reactive power could be calculated to be 2.89 Mvar, 5.77 Mvar, 8.66 Mvar, and 11.55 Mvar according to the working principle of RPC [1]. Reduce $K_{\rm pI1}$ to 0.09 to make the interconnected system in a critical stable state. Other parameters are as listed in Tables I and II. The impedance model of single-phase MMC-RPC and power grid are in three orders, thus the impedance ratio has

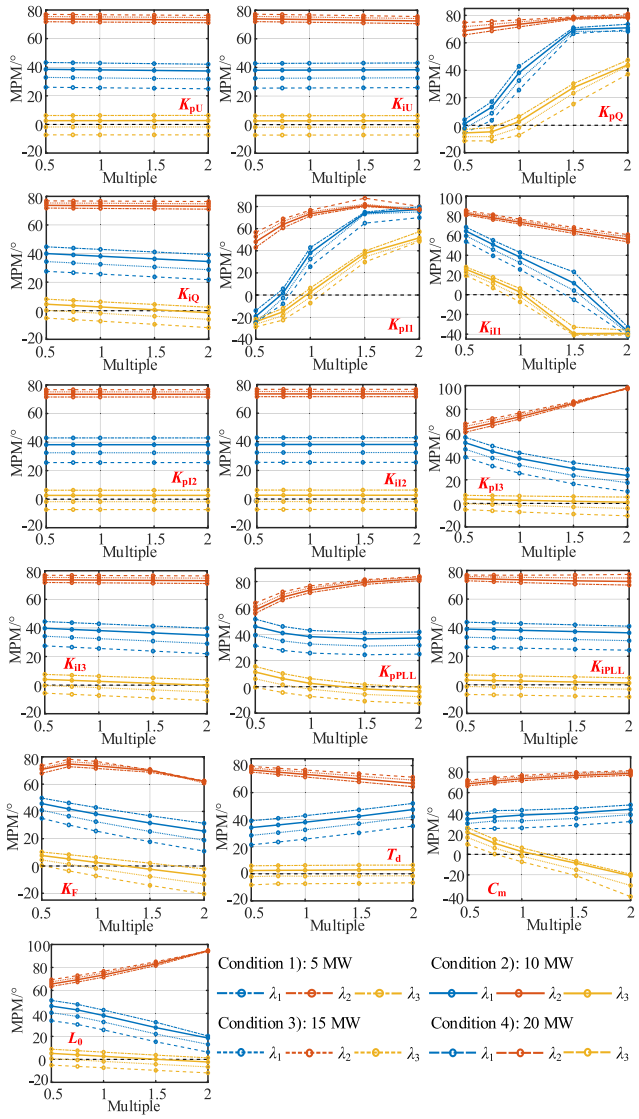

Fig. 11. Changing rules of the MPM of three eigenvalues with different parameters marked in the bottom corner of these figures.

three eigenvalues, λ_1, λ_2, and λ_3. The changing rules of the MPM of three eigenvalues in the above-mentioned four cases are presented in Fig. 11, where the *X*-axis represents the multiple of original parameter values.

Here condition 2) is first analyzed in detail. From the MPM analysis results, it is observed that as follows.

1) The integral coefficient of PLL and parameters of dc voltage control and CCSC have very small impacts on the MPM of three eigenvalues. The time delay T_d has a certain influence on the MPM of λ_1 and λ_2, but has very little effect on the MPM of λ_3, and will not create additional low-frequency oscillations. The proportional coefficient of reactive power control and parameters of fundamental current control may cause instability in λ_1 and λ_3. Other parameters only could cause instability in λ_3. The MPM of λ_2 is always larger than 60°, thus, λ_2 is a strong-damping mode. λ_1 and λ_3 are two weak-damping modes. Besides, λ_3 is always the dominant mode regardless of the parameter values.
2) With the increase of the feedforward coefficient and the proportional coefficients of fundamental current control, the MPM of λ_2 first increases and then decreases within a small range, showing nonmonotonic characteristics. Except for these two parameters and those that have little effect on MPM, with the increase of the other control parameters, the MPM of three eigenvalues show monotonic characteristics, of which parameters of reactive power control and the integral coefficients of the fundamental current control and TCSC separately have consistent influencing rules on the MPM of three eigenvalues, but the proportional coefficients of TCSC and PLL do not.
3) With the increase of submodule capacitance C_m, the MPMs of λ_1 and λ_2 increase. But there is a sharp decline in the MPM of λ_3, which is smaller than 0° when C_m is larger than one limited value indicating system instability is prone to occur. As arm inductance L_0 increases, the MPM of λ_2 increases but the MPMs of λ_1 and λ_3 decrease, and the MPM of λ_3 is smaller than 0° when L_0 exceeds one limited value, indicating that smaller L_0 is beneficial for the system stability. It is widely known that larger C_m or L_0 can reduce internal harmonics, but will also reduce system stability margin according to the above-mentioned analysis. Thus, there will be a tradeoff when designing these two parameters.
4) The sensitivities of different control parameters on the MPM of three eigenvalues are shown in Fig. 12. Since λ_2 is a strong-damping mode, its parameter sensitivity could be ignored. The rankings of key control parameters for λ_1 and λ_3 and corresponding sensitivity values are listed in Table III. It is found that in condition 2) the first three key parameters are the same for λ_1 and λ_3 but a little different in order. The effects of these key parameters

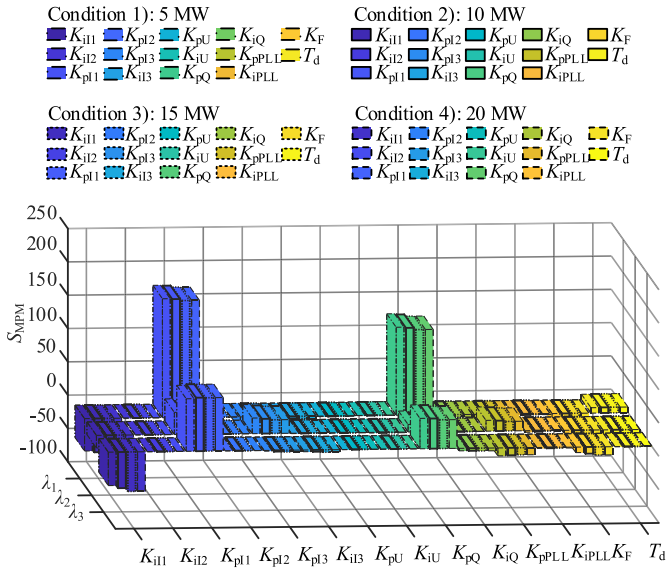

Fig. 12. Comparison of parameter sensitivity under four conditions.

TABLE III
RANKING OF KEY CONTROL PARAMETERS UNDER DIFFERENT CONDITIONS

Condition	Eigenvalue	Key control parameters
1) 5 MW	λ_1	K_{pI1}(178.7) > K_{pQ}(132.1) > K_{iI1}(-48.7) > K_{pI3}(-19.7) > K_F(-12.3)
	λ_3	K_{pI1}(78.9) > K_{iI1}(-50.2) > K_{pQ}(45.6) > K_{pPLL}(-12.0) > K_F(-8.3)
2) 10 MW	λ_1	K_{pI1}(177.9) > K_{pQ}(130.9) > K_{iI1}(-50.1) > K_{pI3}(-20.1) > K_F(-13.9)
	λ_3	K_{pI1}(80.3) > K_{iI1}(-54.2) > K_{pQ}(45.2) > K_{pPLL}(-11.2) > K_F(-10.1)
3) 15 MW	λ_1	K_{pI1}(175.7) > K_{pQ}(128.2) > K_{iI1}(-53.1) > K_{pI3}(-20.9) > K_F(-15.3)
	λ_3	K_{pI1}(80.1) > K_{iI1}(-59.3) > K_{pQ}(43.2) > K_F(-12.2) > K_{pPLL}(-10.7)
4) 20 MW	λ_1	K_{pI1}(171.1) > K_{pQ}(123.3) > K_{iI1}(-56.2) > K_{pI3}(-20.6) > K_F(-16.7)
	λ_3	K_{pI1}(78.6) > K_{iI1}(-55.9) > K_{pQ}(46.3) > K_F(-12.5) > K_{pPLL}(-9.4)

on the MPM of λ_1 and λ_3 are the same, which means that when any one of these key parameters changes, the MPM of λ_1 and λ_3 will change in the same direction, and this is beneficial for improving the system stability by parameter optimization. In particular, λ_3 is always the dominant mode, thus, its high-sensitivity parameters should be optimized with priority. The main function of feedforward control is to introduce ac voltage at PCC into the control system to facilitate real-time tracking speed and accelerate the response speed of the whole system under voltage fluctuation situations. Therefore, the value of K_{F} is closely related to the transient performance of the system. Especially under the low-voltage ride-through situation, the feedforward coefficient affects the transient current characteristics of the system. In addition, in the system design process, feedforward coefficients are often designed according to transient response characteristics or empirical values. The adjustment range of the feedforward coefficient is often limited in practice. Therefore, in this article, K_{F} is suitable to be used as a backup option when other parameters are invalid, which conforms to the general parameter design principles.

5) According to the analysis of key parameters, the ranking of key control loops is fundamental current control > reactive power control > PLL. The proportional and integral coefficients of PLL have similar influencing rules on the MPM of λ_3. Thus, the system stability margin can be improved with a lower bandwidth of PLL. However, the proportional and integral coefficients of fundamental current control or reactive power control both have opposite influencing trends on the MPM of λ_3. Thus, strictly speaking, there is no significant relationship between the bandwidth of these two control loops with the system stability margin.

The above-mentioned analysis reveals the mechanism of the LFOs caused by the interaction of single-phase MMC-RPC and weak traction power grid. And the obtained conclusions can provide useful guidance for the design of system stability. Therein, the parameter optimization guideline for interaction stability improvement between the single-phase MMC-RPC and traction power grid is concluded as

$$\begin{aligned}\text{Increase } K_{\mathrm{pI1}} &> \text{decrease } K_{\mathrm{iI1}} > \text{increase } K_{\mathrm{pQ}} \\ &> \text{decrease } K_{\mathrm{pPLL}} > \text{decrease } K_{\mathrm{F}}.\end{aligned}$$

To illustrate whether the above-proposed conclusions and guidelines are universal for different compensated power levels, conditions 1), 3), and 4) are compared with condition 2) here. From the comparison results shown in Figs. 11 and 12, it is demonstrated that as follows.

1) The changing rules of MPM, dominant and unstable modes are consistent in all four conditions.
2) With the increase of compensated power, the MPM of λ_2 increases, but the MPMs of λ_1 and λ_3 both decrease. Considering λ_2 is a strong-damping mode and λ_1 and λ_3 are both weak-damping modes, it is demonstrated that the system stability can be improved to a higher level with less compensated power.
3) As listed in Table III, the ranking of key control parameters of λ_1 in conditions 1), 3), and 4) are the same as that in condition 2). The ranking of key parameters of λ_3 in condition 1) is the same as that in condition 2). Except for the order of K_{F}, other key parameters of λ_3 in conditions 3) and 4) are also the same as that in condition 2). As the compensated power increases, the sensitivity value of K_{F} increases slightly but is always very close to the sensitivity value of K_{pPLL}. Combined with the previous analysis of K_{F}, here K_{F} is chosen as a backup option, and the abovementioned conclusions and proposed guidelines are still valid.

In conclusion, the obtained parameter optimization guideline for system stability improvement is universal and effective under different compensation power levels in the interconnected system consisting of single-phase MMC-RPC and the traction power grid. However, if the system structure changes, for instance, wiring connection modes, converter topology, or control algorithm, the above-mentioned guidelines are not necessarily appropriate. But the whole set of stability analysis methods is still applicable. According to the research ideas in this article, the guidelines for improving the system stability under other scenarios can also be obtained similarly, which is exactly reflected in the following section.

V. MECHANISM ANALYSIS OF LFOS IN THE SINGLE-PHASE MMC-RPC INTEGRATED VEHICLE-GRID COUPLING SYSTEM

This section will mainly analyze the stability of the single-phase MMC-RPC integrated vehicle-grid system when there are vehicle loads under the right feeder section and MMC-RPC compensates active and reactive power to the right side power grid. To comprehensively study the system stability, this section will first analyze the stability of the vehicle-grid coupling system without single-phase MMC-RPC, and then study the system stability when MMC-RPC is integrated.

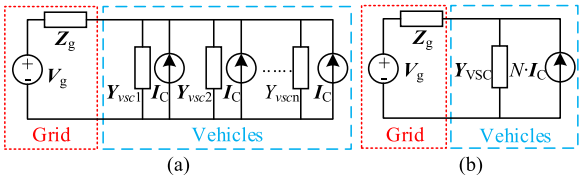

Fig. 13. (a) Equivalent circuit and (b) simplified equivalent circuit of the vehicle-grid coupling system.

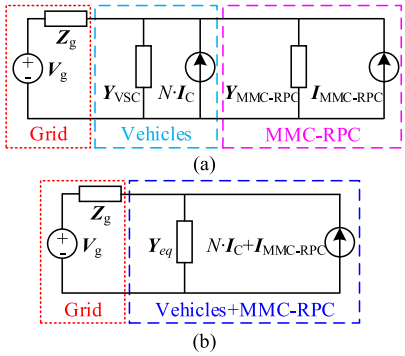

Fig. 14. (a) Equivalent circuit and (b) simplified equivalent circuit of the single-phase MMC-RPC integrated vehicle-grid coupling system.

A. System Equivalence

According to the impedance-based method, the equivalent circuit of the vehicle-grid system is shown in Fig. 13(a), where the power grid is equivalent to a voltage source subsystem and the vehicle loads are equivalent to current source subsystems. Here all vehicles are assumed to be the same, thus, the interconnected system could be further equivalent to the circuit in Fig. 13(b). The equivalent input admittance of the vehicle loads is

$$\boldsymbol{Y}_{\mathrm{VSC}} = N \cdot \boldsymbol{Y}_{vsc} \tag{47}$$

where N is the number of vehicles. $\boldsymbol{Y}_{vsc}$ is the input admittance of one vehicle. The system is stable when these vehicles are powered by an ideal grid, thus, $\boldsymbol{Y}_{vsc}$ has no RHP poles. Hence, the vehicle-grid system is stable only when the total number of counterclockwise encirclements of the critical point $(-1, \mathrm{j}0)$ by the eigen-loci of $\boldsymbol{Z}_{\mathrm{g}}\boldsymbol{Y}_{\mathrm{VSC}}$ equals zero.

After single-phase MMC-RPC is integrated into the vehicle-grid system, the equivalent circuit of the whole system is shown in Fig. 14(a). The vehicles and MMC-RPC could be further equivalent to a current source subsystem, as shown in Fig. 14(b). Equivalent admittance of the whole load is

$$\boldsymbol{Y}_{eq} = \boldsymbol{Y}_{\mathrm{VSC}} + \boldsymbol{Y}_{\mathrm{MMC-RPC}}. \tag{48}$$

The single-phase MMC-RPC integrated vehicle-grid coupling system is stable only when the total number of counterclockwise encirclements of the critical point $(-1, \mathrm{j}0)$ by the eigen-loci of $\boldsymbol{Z}_{\mathrm{g}}\boldsymbol{Y}_{eq}$ equals zero.

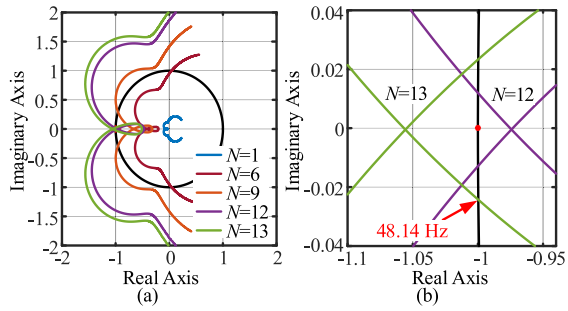

Fig. 15. Nyquist curves when the number of vehicles increases. (a) Full scale. (b) Zoom-in figure.

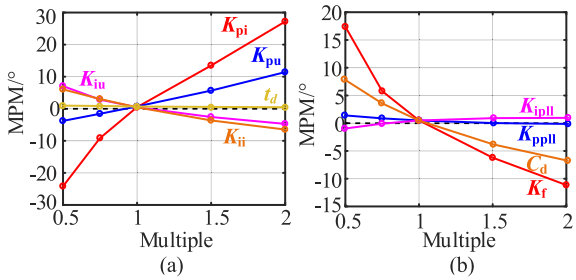

Fig. 16. Changing rules of the MPM of λ_1 with different parameter values of (a) dc voltage control, phase current control, time delay, and (b) PLL, dc-link capacitance, and feedforward coefficient.

B. Stability Analysis of Vehicle-Grid Coupling System Without Single-Phase MMC-RPC

This section will mainly study the stability of the vehicle-grid system when single-phase MMC-RPC is not equipped. All the energy supplied to the vehicles is from the right side traction power grid.

The latest papers have demonstrated that as the number of vehicles N increases, the system stability margin decreases, and LFO around fundamental frequency occurs finally [36]. As shown in Fig. 15, when N increases, three Nyquist curves move toward the left, and the phase margin decreases. Since λ_2 and λ_3 are two strong-damping modes and their Nyquist curves never intersect with the unit circle, these two curves are not plotted here. When $N = 13$, the Nyquist curve of λ_1 encircles the point $(-1, \mathrm{j}0)$, which means that the system will lose stability, and an LFO at 48.14 Hz is prone to happen. Therefore, in the following analysis, 12 vehicles are considered the critical stable condition for studying the system stability.

Fig. 16 shows the changing rules of the MPM of λ_1 when the parameters of vehicle rectifiers change. It can be observed from the results that as follows.

1) Inappropriate control parameters or dc-link capacitance C_{d} may cause system instability and generate LFOs. And the dominant mode is always λ_1.
2) With the decrease of C_{d}, the MPM of λ_1 increases, which indicates that smaller C_{d} benefits the system stability. Besides, the selection of the dc-link capacitor is closely related to the dc-link voltage ripples. The larger the dc-link capacitor, the smaller the dc-link voltage ripples. Therefore, when designing the value of dc-link capacitance, a

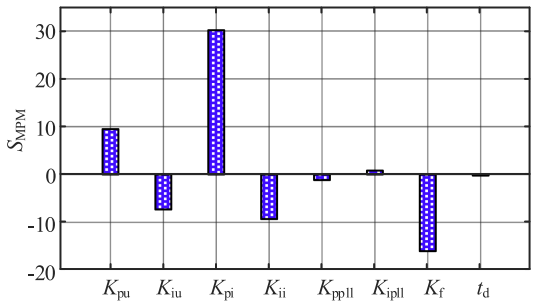

Fig. 17. Parameter sensitivity analysis results of the vehicle-grid system.

compromise shall be made between the system stability and the allowable value of dc voltage ripples.

3) The effects of all parameters on the MPM of λ_1 are monotonic, which is beneficial for improving system stability by optimizing parameters.
4) Fig. 17 shows the control parameter sensitivity analysis results, which demonstrate that the ranking of key parameters of λ_1 is $K_{\rm pi} > K_{\rm f} > K_{\rm pu} > K_{\rm ii} > K_{\rm iu}$.
5) According to the abovementioned key parameters, it is found that the ranking of key control loops is phase current control $>$ dc voltage control. However, the proportional and integral coefficients of current control or dc voltage control both have opposite influences on the MPM of λ_1, which means that strictly speaking, there is no significant relationship between the bandwidth of these two control loops with the system stability margin.

Since all the effects of parameters are monotonic, thus, the parameter sensitivity analysis results could be referred to as the guideline for system stability enhancement. Due to the impacts of feedforward control on the system's transient responses, it is more suitable to be a backup parameter when other parameters are invalid.

The above-mentioned conclusions reveal the mechanism of the LFOs in the vehicle-grid coupling system and provide a series of helpful guidance for the enhancement of the system's small-signal stability. Therein, the parameter optimization guideline can be concluded as

$$\begin{aligned}\text{Increase } K_{\rm pi} &> \text{increase } K_{\rm pu} > \text{decrease } K_{\rm ii} \\ &> \text{decrease } K_{\rm iu} > \text{decrease } K_{\rm f}.\end{aligned}$$

C. Stability Analysis of the Single-Phase MMC-RPC Integrated Vehicle-Grid Coupling System

This section will mainly study the stability of the vehicle-grid system when single-phase MMC-RPC is integrated. The right-side traction power grid and MMC-PRC supply power to the vehicle loads together. And MMC-RPC also compensates the corresponding reactive power to the power grid. Section IV and Section V-B have clarified the key control parameters of single-phase MMC-RPC and vehicle rectifiers, including $K_{\rm pI1}$, $K_{\rm iI1}$, $K_{\rm pQ}$, and $K_{\rm pPLL}$ in the MMC-PRC and $K_{\rm pi}$, $K_{\rm pu}$, $K_{\rm ii}$, and $K_{\rm iu}$ in the vehicle rectifier. In the following, the effects of these parameters on the vehicle-grid coupling system are focused on.

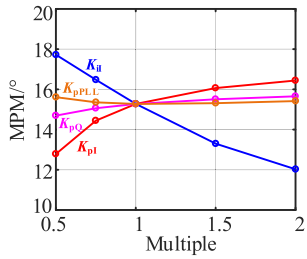

Fig. 18. Changing rules of the MPM of λ_1 with different parameters of single-phase MMC-RPC.

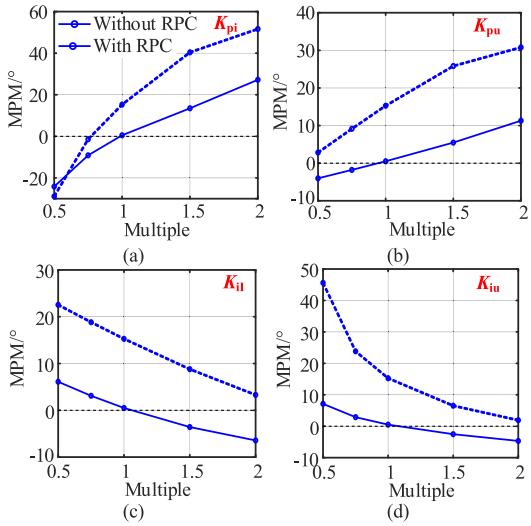

Fig. 19. Changing rules of the MPM of λ_1 with different values of (a) $K_{\rm pi}$, (b) $K_{\rm pu}$, (c), $K_{\rm ii}$, and (d) $K_{\rm iu}$ in the vehicle rectifier.

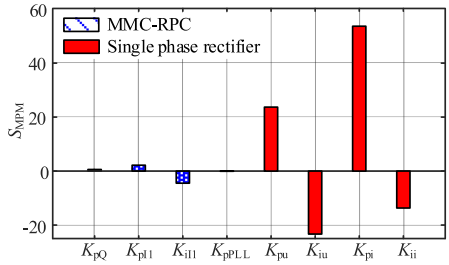

Fig. 20. Parameter sensitivity analysis results of the single-phase MMC-RPC integrated vehicle-grid coupling system.

Fig. 18 and the dashed lines in Fig. 19 separately present the changing rules of the MPM of λ_1 with different parameters of MMC-RPC and the vehicle rectifier. Same as in the last subsection, λ_2 and λ_3 are two strong-damping modes, and their Nyquist curves do not intersect with the unit circle. It is observed from the results that as follows.

1) The dominant mode does not change and is still λ_1 after single-phase MMC-RPC is integrated into the vehicle-grid coupling system.
2) Key parameters of MMC-RPC have small effects on the MPM, and key parameters of the vehicle rectifier have relatively large impacts on the MPM. The sensitivity analysis results of these eight parameters are shown in Fig. 20. The

ranking of the sensitivity values is $K_{\mathrm{pi}} > K_{\mathrm{pu}} > K_{\mathrm{iu}} > K_{\mathrm{ii}} > K_{\mathrm{pI1}} > K_{\mathrm{iI1}} > K_{\mathrm{pQ}} > K_{\mathrm{pPLL}}$. Combining the results of MPM analysis and parameter sensitivity analysis, the key parameters of the vehicle rectifier have much larger impacts on the stability of the single-phase MMC-RPC integrated vehicle-grid system than that of MMC-RPC.

To compare the effects of the key parameters of the vehicle rectifier on the system stability with and without single-phase MMC-RPC, the effects of key parameters on the MPM of λ_1 of the vehicle-grid system without MMC-RPC are also plotted in Fig. 19(solid lines). It is indicated that as follows.

1) The MPM of λ_1 is increased to a certain extent when single-phase MMC-RPC is integrated, which means that the access of MMC-RPC improves the stability of the vehicle-grid coupling system.
2) Key parameters of the vehicle rectifier have similar impacts on the MPM of λ_1 with and without MMC-RPC. In other words, both the MPMs of λ_1 change monotonically in the same direction when some key parameter increases.
3) Comparing the sensitivity analysis results in Figs. 17 and 20, the sensitivity orders of K_{pu} and K_{pi} are the same, while the sensitivity orders of K_{iu} and K_{ii} are opposite in the vehicle-grid system with and without MMC-RPC, which also highlights the significance of the stability analysis of the entire interconnected system.
4) Comparing the sensitivity analysis results of single-phase MMC-RPC in Figs. 12 and 20, it is found that the sensitivity orders of K_{pQ} and K_{pPLL} are the same, while the sensitivity orders of K_{iI1} and K_{pIi} are opposite. Comparing the MPM analysis results of MMC-RPC in Figs. 11 and 18, it is found that the effects of key parameters of MMC-RPC on the MPM values are all monotonic. And the changing directions of the MPM of dominant modes are the same with the increase of key parameters of MMC-RPC, which indicates that optimizing the parameters of MMC-RPC is beneficial for all the working scenarios discussed in Sections IV and V.

The above-mentioned analysis unveils the mechanism of the LFOs in the single-phase MMC-RPC integrated vehicle-grid coupling system. The obtained conclusions can also provide a series of useful guidance for the small-signal stability improvement of this interconnected system. Among them, the parameter optimization guideline is concluded as

$$\begin{aligned}\text{Increase } K_{\mathrm{pi}} &> \text{increase } K_{\mathrm{pu}} > \text{decrease } K_{\mathrm{iu}} \\ &> \text{decrease } K_{\mathrm{ii}} > \text{decrease } K_{\mathrm{iI1}} > \text{increase } K_{\mathrm{pI1}} \\ &> \text{increase } K_{\mathrm{pQ}} > \text{decrease } K_{\mathrm{pPLL}}.\end{aligned}$$

D. Further Discussion About the Effects of Single-Phase MMC-RPC

To further study the effects of single-phase MMC-RPC on the stability of the vehicle-grid coupling system, this section will discuss the effects of different control loops and compensated power levels, respectively.

The previous studies only analyzed the influence of parameters on the system stability when varying within a reasonable range but did not study how the control loops influence the system phase margin. Fig. 21 presents the changing rules of λ_1 when different control loops are added one by one. It is demonstrated in the results that dc voltage control would slightly reduce the system phase margin. All other control loops can improve the system stability to a certain extent, of which the fundamental current control, PLL, and TCSC have obvious effects, and the effects of CCSC could be ignored.

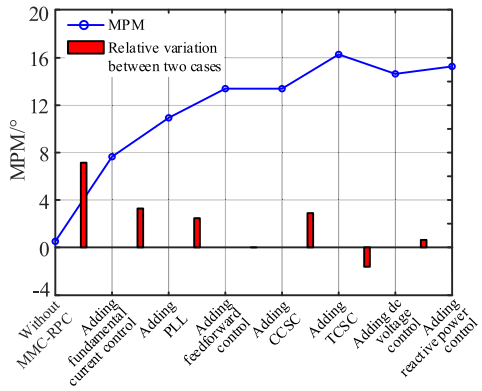

Fig. 21. Changing rules of the MPM of λ_1 with different control loops of single-phase MMC-RPC.

TABLE IV
COMPENSATED POWER VALUES IN EIGHT CASES

Case	Value	Case	Value
1)	Without MMC-RPC	5)	P=22MW, Q=6Mvar
2)	P=1MW, Q=13Mvar	6)	P=22MW, Q=0Mvar
3)	P=11MW, Q=13Mvar	7)	P=22MW, Q=-6Mvar
4)	P=22MW, Q=13Mvar	8)	P=22MW, Q=-10Mvar

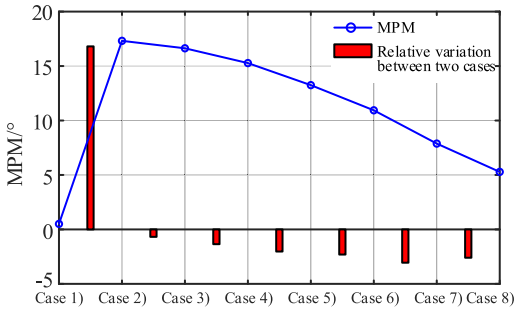

Fig. 22. Changing rules of the MPM of λ_1 with different compensated power of single-phase MMC-RPC.

Eight cases are considered here to study the influence of the compensated power by single-phase MMC-RPC. The specific power values are listed in Table IV. Variations of the MPM of λ_1 with different compensated power are plotted in Fig. 22. It is demonstrated in the results that as follows.

1) When the compensated reactive power is fixed, the phase margin increases with the decrease of active power.
2) When the compensated active power is fixed, the phase margin increases with the increase of inductive reactive power and the decrease of capacitive reactive power.
3) Compensated reactive power has a larger impact on system stability than active power.

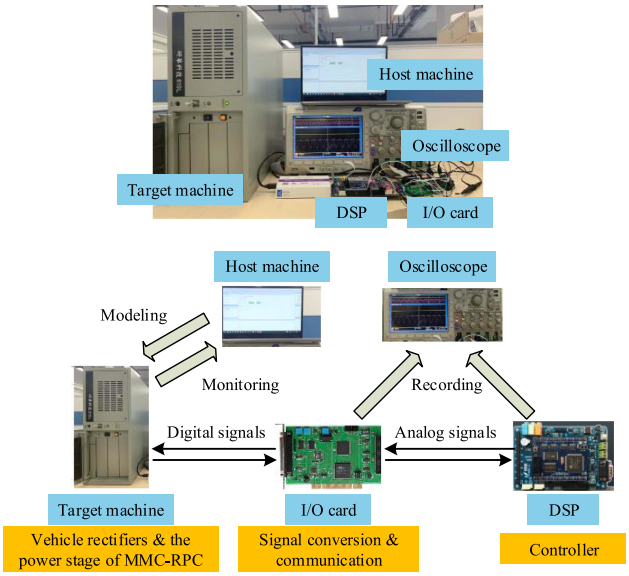

Fig. 23. Photograph of the HIL platform.

4) The stability margin of the vehicle-grid system can be significantly enhanced with MMC-RPC regardless of the control loops and compensated power of MMC-RPC.

The above-mentioned conclusions indicate that only reactive compensation has better stability improvement performance than the combination of active and reactive compensation. In other words, single-phase MMC-RPC can raise the system stability margin to a higher level if only working as a STATCOM. However, the compensated power is determined by the demand of the traction system and cannot be randomly designed according to the stability, unless other compensation equipment is additionally installed.

VI. Experimental Verification

To prove the effectiveness of the theoretical analysis of the system stability, a detailed real-time digital simulation model of the single-phase MMC-RPC integrated vehicle-grid system, as shown in Fig. 1, is constructed in a HIL platform. The photograph and setup of the HIL platform are shown in Fig. 23. Therein, the control algorithm of the single-phase MMC-RPC is implemented in a DSP (TMS320F28335) controller and the other system elements operate in real-time with a step size of 8 μs in the target machine. The conversion and communication of the signals between the target machine and the DSP peripheral circuit are realized by multifunction I/O cards Humusoft MF624. The oscilloscope is used to monitor and record the waveforms and data of voltages and currents in real-time. Parameters of the power stage and control system are adopted, as listed in Tables I and II.

A. Verification of the Interaction Stability Between Single-Phase MMC-RPC and Traction Power Grid

To verify the effectiveness of the small-signal stability analysis between the single-phase MMC-RPC and traction power grid, three cases are considered here: Case 1): $K_{\mathrm{pI1}} = 0.09$ and $K_{\mathrm{iI1}} = 2.5$. Case 2): $K_{\mathrm{pI1}} = 0.08$ and $K_{\mathrm{iI1}} = 2.5$. Case 3): $K_{\mathrm{pI1}} = 0.08$ and $K_{\mathrm{iI1}} = 2.2$.

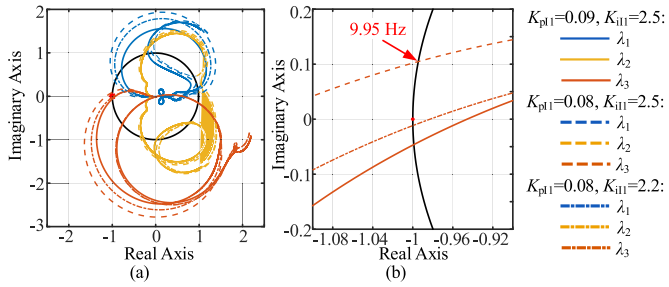

Fig. 24. Nyquist curves of three eigenvalues. (a) Full scale. (b) Zoom-in figure.

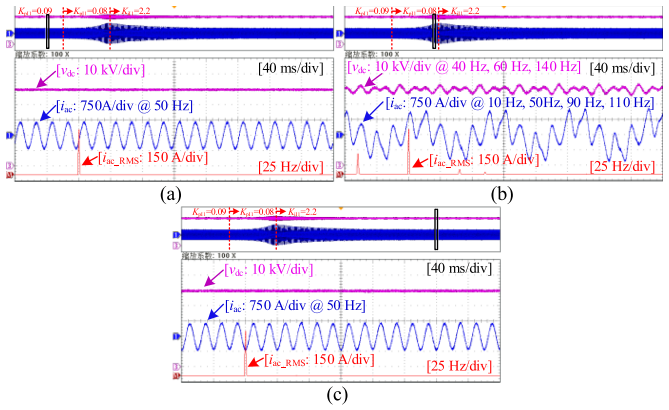

Fig. 25. Waveforms of ac current and dc voltage in (a) Case 1), (b) Case 2), and (c) Case 3).

The initial parameter values of fundamental current control are $K_{\mathrm{pI1}} = 0.09$ and $K_{\mathrm{iI1}} = 2.5$ in Case 1). Nyquist curves of three eigenvalues are shown in Fig. 24. As K_{pI1} decreases, the Nyquist curves move toward the left. When K_{pI1} equals 0.09, the Nyquist curves do not encircle $(-1, \mathrm{j}0)$, which means that the system is stable. When K_{pI1} equals 0.08 in Case 2), the Nyquist curve of λ_3 encircles $(-1, \mathrm{j}0)$ and the MPM is smaller than zero, which indicates that the system is unstable and an LFO at 9.95 Hz is prone to occur. At this time, decrease K_{iI1} to 2.2 in Case 3). The MPM of λ_3 increases and is larger than zero again, thus, the system will return to stability.

It is shown in Fig. 25(a) that the system is stable with the initial values of K_{pI1} and K_{iI1} in Case 1). When parameter K_{pI1} changes from 0.09 to 0.08 at 10 s in Case 2), HIL results presented in Fig. 25(b) show that the ac current and dc voltage begin to diverge, and the oscillation frequency is 10 Hz at the ac side and 40 Hz at the dc side. Corresponding harmonics are also generated at the ac and dc sides. The oscillation frequencies marked in the figures also coincide with the predicted results. In Case 3), when K_{iI1} changes from 2.5 to 2.2, the system returns to a stable state. Table V shows the total harmonic distortion (THD) of grid current and the fluctuation of dc voltage for the cases in Fig. 25. The above-mentioned HIL results are consistent with the previous analysis, which verifies that increasing K_{pI1} or decreasing K_{iI1} could enhance system stability.

TABLE V
PERFORMANCE COMPARISON OF ELECTRICAL QUANTITIES

Case	THD of i_{ac}	Fluctuation of v_{dc}
1)	2.41%	±54V
2)	18.24%	±2110V
3)	2.53%	±60V

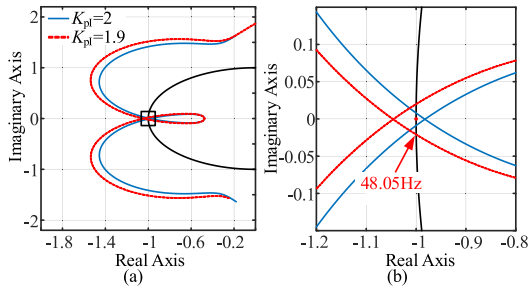

Fig. 26. Nyquist curves of λ_1 with different values of K_{pi}. (a) Full scale. (b) Zoom-in figure.

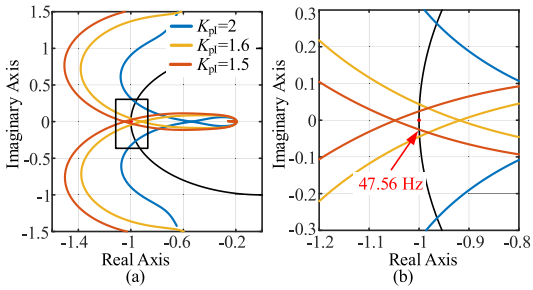

Fig. 27. Nyquist curves with different values of K_{pi}. (a) Full scale. (b) Zoom-in figure.

B. Verification of the Critical Value of K_{pi} With and Without Single-Phase MMC-RPC

To verify the improvement effects brought by single-phase MMC-RPC to the vehicle-grid system, the change of the critical value of K_{pi} with and without MMC-RPC is studied. Four cases are considered here: Case 4): $K_{pi} = 2$ without MMC-RPC. Case 5): $K_{pi} = 1.9$ without MMC-RPC. Case 6): $K_{pi} = 1.6$ with MMC-RPC. Case 7): $K_{pi} = 1.5$ with MMC-RPC.

When MMC-RPC is not integrated into the vehicle-grid coupling system, the initial value of the proportional coefficient K_{pi} of phase current control of the vehicle rectifier is 2. As shown in Fig. 26, with the decrease of K_{pi}, the Nyquist curve of λ_1 moves toward the left. When K_{pi} equals 1.9 in Case 2), the Nyquist curve encircles (−1, j0) and the MPM is smaller than zero, indicating that the system is unstable and an LFO at 48.05 Hz is prone to occur. After MMC-RPC is integrated into the vehicle-grid coupling system, the initial value of K_{pi} is also 2. As shown in Fig. 27, when K_{pi} decreases, the phase margin is reduced. When K_{pi} changes from 1.6 to 1.5, the Nyquist curve encircles (−1, j0), indicating the system will lose stability, and the oscillation frequency is 47.56 Hz.

HIL results presented in Fig. 28(a) and (b) show that when single-phase MMC-RPC is not integrated into the vehicle-grid system, the system is stable in Case 4) but unstable in Case 5). The oscillation frequencies at the ac side are 48 Hz, 52 Hz, and 148 Hz, which is consistent with the predicted results. Thus the critical value of K_{pi} for system stability is 2. HIL results presented in Fig. 28(c) and (d) show that when single-phase MMC-RPC is integrated, the system is stable in Case 6) but loses stability in Case 7). The ac-side current gradually diverges, and harmonics at 48 Hz, 52 Hz, and 148 Hz are generated simultaneously. Thus, the critical value of K_{pi} becomes 1.6. Table VI shows the THD of grid current and the fluctuation of dc voltage for the cases in Fig. 28. Comparing these four cases, HIL results are consistent with the previous theoretical analysis results, thus it is verified that the integration of single-phase MMC-RPC enlarges the feasible regions of control parameters of vehicle rectifiers. Actually, the feasible regions of other parameters are also enlarged and could be proved similarly.

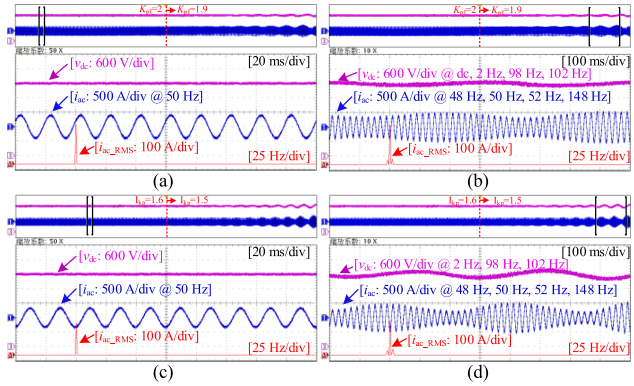

Fig. 28. Waveforms of ac current and dc voltage in (a) Case 4), (b) Case 5), (b) Case 6), and (c) Case 7).

TABLE VI
PERFORMANCE COMPARISON OF ELECTRICAL QUANTITIES

Case	THD of i_{ac}	Fluctuation of v_{dc}
4)	2.49%	±10V
5)	18.93%	±77V
6)	2.52%	±10V
7)	24.80%	±118V

C. Verification of the Critical Number of Vehicles With and Without Single-Phase MMC-RPC

To verify the effects of single-phase MMC-RPC on the critical number of vehicles, four cases of considered similarly: Case 8): $N = 12$ without MMC-RPC. Case 9): $N = 13$ without MMC-RPC. Case 10): $N = 19$ with MMC-RPC. Case 11): $N = 20$ with MMC-RPC.

Fig. 15 has shown that when MMC-RPC is not integrated, the critical number N of vehicles that can operate steadily is 12. Fig. 29 shows that when MMC-RPC is integrated, the Nyquist curves move toward the left when the number of vehicles N increases. And when N equals 19, the Nyquist curve does not encircle (−1, j0), meaning that the system is stable. When N equals 20, the Nyquist curves encircle (−1, j0), indicating that the system will change from a stable to an unstable state, and the corresponding oscillation frequency is 47.79 Hz.

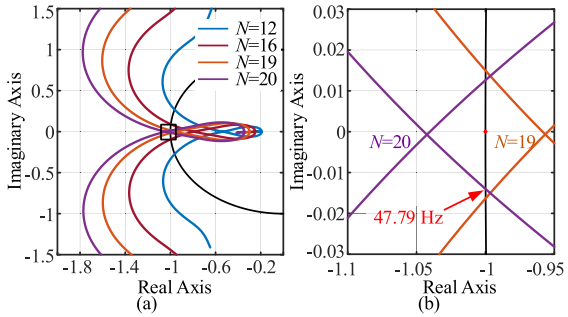

Fig. 29. Nyquist curves when the number of vehicles increases. (a) Full scale. (b) Zoom-in figure.

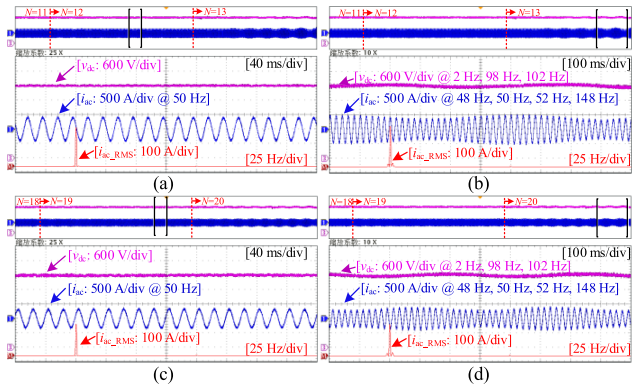

Fig. 30. Waveforms of ac current and dc voltage in (a) Case 8), (b) Case 9), (b) Case 10), and (c) Case 11).

TABLE VII
PERFORMANCE COMPARISON OF ELECTRICAL QUANTITIES

Case	THD of i_{ac}	Fluctuation of v_{dc}
8)	3.62%	±15V
9)	15.49%	±51V
10)	4.45%	±18V
11)	14.35%	±48V

HIL results presented in Fig. 30(a) and (b) show that when single-phase MMC-RPC is not integrated into the vehicle-grid system, the system is stable in Case 8) but unstable in Case 9). Thus, the critical value of N for system stability is 12. However, when single-phase MMC-RPC is integrated, the HIL results of Case 10) and Case 11), which are presented in Fig. 30(c) and (d), show that the critical value of N increases to 19. Table VII shows the THD of grid current and the fluctuation of dc voltage for the cases in Fig. 30. The above-mentioned HIL results are consistent with the theoretical analysis results and verify that the integration of single-phase MMC-RPC allows more vehicles to operate under the same feeder at the same time.

Combined with the verification in Section VI-B, it is proved that the integration of single-phase MMC-RPC can effectively enhance the stability of the vehicle-grid coupling system.

VII. CONCLUSION

This article develops accurate third-order ac admittance models of single-phase MMC-RPC and vehicle rectifiers, taking into account the effects of complete frequency coupling, grid impedance coupling, and the initial phase of the reference frame. It is revealed that the above-mentioned three factors have non-negligible impacts on the low-frequency range of ac admittances and, thus, are significant for the LFO mechanism analysis in this article.

This article proposes a modal analysis method based on MPM and parameter sensitivity and combined with the GNC. LFO mechanism analyses under the following three working scenarios are conducted. 1) The interconnected system composed of single-phase MMC-RPC and traction power grid; 2) The vehicle-grid coupling system without MMC-RPC; 3) The single-phase MMC-RPC integrated vehicle-grid coupling system. It is pointed out that LFOs around 10 Hz or 48 Hz may happen in the above-mentioned three scenarios due to inappropriate system parameters, and sideband oscillations are also generated due to frequency coupling effects. Dominant modes, key control parameters, and key control loops are clarified, and a series of guidelines are proposed for system stability enhancement. It is demonstrated that the fundamental current, reactive power controls, and PLL of single-phase MMC-RPC and phase current and dc voltage controls of vehicle rectifiers make a significant difference in the low-frequency stability.

This article also reveals that the impedance of vehicle rectifiers is reshaped by introducing the single-phase MMC-RPC, which results in significant changes in the eigenvalue loci. The access of single-phase MMC-RPC enlarges the feasible regions of vehicle rectifier parameters and increases the critical number of vehicles that can operate under the same feeder section. In addition, the effects of control loops and power flow of single-phase MMC-RPC are studied. It is unveiled that all control loops except the dc voltage control loop or compensating less active power or more inductive reactive power to the traction power grid could effectively improve system stability. It is also revealed that only reactive compensation has better stability improvement performance than the combination of active and reactive compensation.

In summary, the systematical research of the single-phase MMC-RPC integrated vehicle-grid system provides an insight into the mechanism of the LFO and a theoretical basis for the stability design and optimization of general traction power supply systems. The proposed impedance modeling method of single-phase MMC will be of significant value in the stability analysis of systems based on single-phase MMC, such as isolated dc/dc transformers [51], single-phase energy storage systems [52], and single-phase STATCOM [53]. In addition, the proposed frequency-domain GNC-based modal analysis method is equally applicable for any other MIMO system.

REFERENCES

[1] A. Luo, C. Wu, J. Shen, Z. Shuai, and F. Ma, "Railway static power conditioners for high-speed train traction power supply systems using three-phase V/V transformers," *IEEE Trans. Power Electron.*, vol. 26, no. 10, pp. 2844–2856, Oct. 2011.

[2] Y. Mochinaga, Y. Hisamizu, M. Takeda, T. Miyashita, and K. Hasuike, "Static power conditioner using GTO converters for AC electric railway," in *Proc. IEEE Power Convers. Conf.*, 1993, pp. 641–646.

[3] F. Ma, A. Luo, X. Xu, H. Xiao, C. Wu, and W. Wang, "A simplified power conditioner based on half-bridge converter for high-speed railway system," *IEEE Trans. Ind. Electron.*, vol. 60, no. 2, pp. 728–738, Feb. 2013.

[4] D. Zhang, Z. Zhang, W. Wang, and Y. Yang, "Negative sequence current optimizing control based on railway static power conditioner in V/v traction power supply system," *IEEE Trans. Power Electron.*, vol. 31, no. 1, pp. 200–212, Jan. 2016.

[5] S. M. Mousavi Gazafrudi, A. Tabakhpour Langerudy, E. F. Fuchs, and K. Al-Haddad, "Power quality issues in railway electrification: A comprehensive perspective," *IEEE Trans. Ind. Electron.*, vol. 62, no. 5, pp. 3081–3090, May 2015.

[6] A. Luo, F. Ma, C. Wu, S. Q. Ding, Q. C. Zhong, and Z. K. Shuai, "A dual-loop control strategy of railway static power regulator under V/V electric traction system," *IEEE Trans. Power Electron.*, vol. 26, no. 7, pp. 2079–2091, Jul. 2011.

[7] F. Ma et al., "A railway traction power conditioner using modular multilevel converter and its control strategy for high-speed railway system," *IEEE Trans. Transp. Electrific.*, vol. 2, no. 1, pp. 96–109, Mar. 2016.

[8] J. Min, F. Ma, Q. Xu, Z. He, A. Luo, and A. Spina, "Analysis, design, and implementation of passivity-based control for multilevel railway power conditioner," *IEEE Trans. Ind. Informat.*, vol. 14, no. 2, pp. 415–425, Feb. 2018.

[9] L. Liu and N. Dai, "Hybrid railway power conditioner based on half-bridge modular multilevel converter," in *Proc. IEEE Energy Convers. Congr. Expo.*, 2016, pp. 1–7.

[10] Z. He, H. Hu, Y. Zhang, and S. Gao, "Harmonic resonance assessment to traction power-supply system considering train model in China high-speed railway," *IEEE Trans. Power. Del.*, vol. 29, no. 4, pp. 1735–1743, Aug. 2014.

[11] Z. Liu, G. Zhang, and Y. Liao, "Stability research of high-speed railway EMUs and traction network cascade system considering impedance matching," *IEEE Trans. Ind. Appl.*, vol. 52, no. 5, pp. 4315–4326, Sep./Oct. 2016.

[12] H. Hu, Y. Shao, L. Tang, J. Ma, Z. He, and S. Gao, "Overview of harmonic and resonance in railway electrification systems," *IEEE Trans. Ind. Appl.*, vol. 54, no. 5, pp. 5227–5245, Sep./Oct. 2018.

[13] H. Hu, Y. Zhou, X. Li, and K. Lei, "Low-frequency oscillation in electric railway depot: A comprehensive review," *IEEE Trans. Power Electron.*, vol. 36, no. 1, pp. 295–314, Jan. 2021.

[14] J. Freytes et al., "Improving small-signal stability of an MMC with CCSC by control of the internally stored energy," *IEEE Trans. Power Del.*, vol. 33, no. 1, pp. 429–439, Feb. 2018.

[15] X. Wang and F. Blaabjerg, "Harmonic stability in power electronic-based power systems: Concept, modeling, and analysis," *IEEE Trans. Smart Grid*, vol. 10, no. 3, pp. 2858–2870, May 2019.

[16] L. Xiong, X. Liu, Y. Liu, and F. Zhuo, "Modeling and stability issues of voltage-source converter dominated power systems: A review," *CSEE J. Power Energy Syst.*, vol. 8, no. 6, pp. 1530–1549, Nov. 2022, 2020.

[17] H. Wang, M. Wu, and J. Sun, "Analysis of low-frequency oscillation in electric railways based on small-signal modeling of vehicle-grid system in dq frame," *IEEE Trans. Power Electron.*, vol. 30, no. 9, pp. 5318–5330, Sep. 2015.

[18] H. Hu, H. Tao, F. Blaabjerg, X. Wang, Z. He, and S. Gao, "Train-network interactions and stability evaluation in high-speed railways–Part I: Phenomena and modeling," *IEEE Trans. Power Electron.*, vol. 33, no. 6, pp. 4627–4642, Jun. 2018.

[19] Y. Liao, Z. Liu, H. Zhang, and B. Wen, "Low-frequency stability analysis of single-phase system with dq-frame impedance approach-Part I: Impedance modeling and verification," *IEEE Trans. Ind. Appl.*, vol. 54, no. 5, pp. 4999–5011, Sep./Oct. 2018.

[20] K. Jiang, C. Zhang, and X. Ge, "Low-frequency oscillation analysis of the train-grid system based on an improved forbidden-region criterion," *IEEE Trans. Ind. Appl.*, vol. 54, no. 5, pp. 5064–5073, Sep./Oct. 2018.

[21] H. Tao, H. Hu, X. Wang, F. Blaabjerg, and Z. He, "Impedance-based harmonic instability assessment in a multiple electric trains and traction network interaction system," *IEEE Trans. Ind. Appl.*, vol. 54, no. 5, pp. 5083–5096, Sep./Oct. 2018.

[22] Y. Zhou, H. Hu, X. Yang, J. Yang, Z. He, and S. Gao, "Low frequency oscillation traceability and suppression in railway electrification systems," *IEEE Trans. Ind. Appl.*, vol. 55, no. 6, pp. 7699–7711, Nov./Dec. 2019.

[23] H. Zhang, Z. Liu, S. Wu, and Z. Li, "Input impedance modeling and verification of single-phase voltage source converters based on harmonic linearization," *IEEE Trans. Power Electron.*, vol. 34, no. 9, pp. 8544–8554, Sep. 2019.

[24] Y. Liu, S. Wu, X. Meng, and Z. Liu, "SISO equivalent impedance modeling of vehicle network system in harmonic domain considering harmonic coupling," *Power Syst. Technol.*, vol. 46, no. 4, pp. 1594–1604, Apr. 2022.

[25] S. Cheng, L. Ma, X. Ge, L. Peng, and H. Liu, "Low-frequency oscillation analysis in train-traction power supply system using an SISO voltage loop model," *IEEE Trans. Transp. Electrific.*, vol. 8, no. 1, pp. 636–648, Mar. 2022.

[26] Y. Hong, Z. Shuai, H. Cheng, C. Tu, Y. Li, and Z. J. Shen, "Stability analysis of low-frequency oscillation in train-network system using RLC circuit model," *IEEE Trans. Transp. Electrific.*, vol. 5, no. 2, pp. 502–514, Jun. 2019.

[27] P. Pan, H. Hu, X. Yang, F. Blaabjerg, X. Wang, and Z. He, "Impedance measurement of traction network and electric train for stability analysis in high-speed railways," *IEEE Trans. Power Electron.*, vol. 33, no. 12, pp. 10086–10100, Dec. 2018.

[28] H. Hu, P. Pan, Y. Song, and Z. He, "A novel controlled frequency band impedance measurement approach for single-phase railway traction power system," *IEEE Trans. Ind. Electron.*, vol. 67, no. 1, pp. 244–253, Jan. 2020.

[29] I. Tasiu, Z. Liu, S. Wu, W. Yu, M. Al-Barashi, and J. O. Ojo, "Review of recent control strategies for the traction converters in high-speed train," *IEEE Trans. Transp. Electrific.*, vol. 8, no. 2, pp. 2311–2333, Jun. 2022.

[30] G. Zhang, Z. Liu, S. Yao, Y. Liao, and C. Xiang, "Suppression of low-frequency oscillation in traction network of high-speed railway based on auto-disturbance rejection control," *IEEE Trans. Transp. Electrific.*, vol. 2, no. 2, pp. 244–255, Jun. 2016.

[31] Z. Liu, Z. Geng, and X. Hu, "An approach to suppress low frequency oscillation in the traction network of high-speed railway using passivity-based control," *IEEE Trans. Power Syst.*, vol. 33, no. 4, pp. 3909–3918, Jul. 2018.

[32] Z. Liu, Z. Geng, S. Wu, X. Hu, and Z. Zhang, "A passivity-based control of Euler-Lagrange model for suppressing voltage low-frequency oscillation in high-speed railway," *IEEE Trans. Ind. Informat.*, vol. 15, no. 10, pp. 5551–5560, Oct. 2019.

[33] H. Hu, Y. Zhou, J. Yang, Z. He, and S. Gao, "A practical approach to mitigate low-frequency oscillation in railway electrification systems," *IEEE Trans. Power Electron.*, vol. 33, no. 10, pp. 8198–8203, Oct. 2018.

[34] H. Hu, Z. He, and S. Gao, "Passive filter design for China high-speed railway with considering harmonic resonance and characteristic harmonics," *IEEE Trans. Power. Del.*, vol. 30, no. 1, pp. 505–514, Feb. 2015.

[35] Z. Liu, X. Hu, and Y. Liao, "Vehicle-grid system stability analysis based on norm criterion and suppression of low-frequency oscillation with MMC-STATCOM," *IEEE Trans. Transp. Electrific.*, vol. 4, no. 3, pp. 757–766, Sep. 2018.

[36] S. Wu, Z. Liu, Z. Li, H. Zhang, and X. Hu, "Impedance modeling and stability analysis in vehicle-grid system with CHB-STATCOM," *IEEE Trans. Power Syst.*, vol. 35, no. 4, pp. 3026–3039, Jul. 2020.

[37] S. Wu and Z. Liu, "Low-frequency stability analysis of vehicle-grid system with active power filter based on dq-frame impedance," *IEEE Trans. Power Electron.*, vol. 36, no. 8, pp. 9027–9040, Aug. 2021.

[38] S. Wu, J. Jatskevich, Z. Liu, and B. Lu, "Admittance decomposition for assessment of APF and STATCOM impact on the low-frequency stability of railway vehicle-grid systems," *IEEE Trans. Power Electron.*, vol. 37, no. 12, pp. 15425–15441, Dec. 2022.

[39] J. Sun and H. Liu, "Sequence impedance modeling of modular multilevel converters," *IEEE J. Emerg. Sel. Topics Power Electron.*, vol. 5, no. 4, pp. 1427–1443, Dec. 2017.

[40] J. Lyu, Zhang X, X. Cai, and M. Molinas, "Harmonic state-space based small-signal impedance modeling of modular multilevel converter with consideration of internal harmonic dynamics," *IEEE Trans. Power Electron.*, vol. 34, no. 3, pp. 2134–2148, Mar. 2019.

[41] C. Zhang, M. Molinas, A. Rygg, J. Lyu, and X. Cai, "Harmonic transfer-function-based impedance modeling of a three-phase VSC for asymmetric ac grid stability analysis," *IEEE Trans. Power Electron.*, vol. 34, no. 12, pp. 12552–12566, Dec. 2019.

[42] P. Guo et al., "Analysis and control of modular multilevel converter with split energy storage for railway traction power conditioner," *IEEE Trans. Power Electron.*, vol. 35, no. 2, pp. 1239–1255, Feb. 2020.

[43] L. Li, Z. Zhou, N. Dai, K. Lao, and Y. Song, "Interpolated phase-shifted PWM for harmonics suppression of multilevel hybrid railway power conditioner in traction power supply system," *IEEE Trans. Transp. Electrific.*, vol. 8, no. 1, pp. 898–908, Mar. 2022.

[44] J. Yuan, F. Xiao, C. Zhang, Z. Li, and Y. Zhong, "A hybrid negative current compensation system for high-speed railway power system," in *Proc. IEEE Appl. Power Electron. Conf. Expo.*, 2018, pp. 1461–1466.
[45] J. Shang, N. Dai, B. Wang, and H. Chen, "Railway power conditioner based on delta-connected modular multilevel converter," in *Proc. IEEE Energy Convers. Congr. Expo.*, 2016, pp. 1–7.
[46] C. Guo, P. Cui, and C. Zhao, "Optimization and configuration of control parameters to enhance small signal stability of hybrid LCC-MMC HVDC system," *J. Modern Power Syst. Clean Energy*, vol. 10, no. 1, pp. 213–221, Jan. 2022.
[47] P. Li et al., "DC impedance modeling and design-oriented harmonic stability analysis of MMC-PCCF-based HVDC system," *IEEE Trans. Power Electron.*, vol. 37, no. 4, pp. 4301–4319, Apr. 2022.
[48] E. Ebrahimzadeh, F. Blaabjerg, X. Wang, and C. L. Bak, "Bus participation factor analysis for harmonic instability in power electronics based power systems," *IEEE Trans. Power Electron*, vol. 33, no. 12, pp. 10341–10351, Dec. 2018.
[49] Y. Liao, X. Wang, and X. Wang, "Frequency-domain participation analysis for electronic power systems," *IEEE Trans. Power Electron*, vol. 37, no. 3, pp. 2531–2537, Mar. 2022.
[50] Y. Li et al., "Stability analysis and location optimization method for multiconverter power systems based on nodal admittance matrix," *IEEE J. Emerg. Sel. Topics Power Electron.*, vol. 9, no. 1, pp. 529–538, Feb. 2021.
[51] B. Zhao, Q. Song, J. Li, Y. Wang, and W. Liu, "High-frequency-link modulation methodology of dc-dc transformer based on modular multilevel converter for HVDC application: Comprehensive analysis and experimental verification," *IEEE Trans. Power Electron.*, vol. 32, no. 5, pp. 3413–3424, May 2017.
[52] Z. Ma, F. Gao, C. Zhang, W. Li, and D. Niu, "Variable dc-link voltage regulation of single-phase MMC battery energy-storage system for reducing additional charge throughput," *IEEE Trans. Power Electron.*, vol. 36, no. 12, pp. 14267–14281, Dec. 2021.
[53] T. Isobe, H. Funato, H. Kobayashi, and K. Yamaichi, "Experimental verification of capacitance reduction in MMC-based STATCOM," in *Proc. IEEE Energy Convers. Congr. Expo.*, 2016, pp. 1–7.

Pengkun Li (Graduate Student Member, IEEE) received the B.S. degree in electrical engineering from Beijing Jiaotong University, Beijing, China, in 2017. He is currently working toward the Ph.D. degree in electrical engineering with Xi'an Jiaotong University, Xi'an, China.

His research interests include modeling, control, and small-signal harmonic stability analysis of power electronic based power systems.

Yue Wang (Member, IEEE) received the B.S. degree from Xi'an Jiaotong University, Xi'an, China, in 1993, the M.S. degree from Beijing Jiaotong University, Beijing, China, in 1999, and the Ph.D. degree from Xi'an Jiaotong University, in 2003, all in electrical engineering.

From 1993 to 1996, he was an Electrical Engineer with Xi'an Power Electronics Technology Research Institute. He is currently a Full Professor with the School of Electrical Engineering, Xi'an Jiaotong University. His research interests include wireless power transfer, active power filters, multilevel converters, and HVdc.

Yi Liu received the B.S. degree in electrical engineering and automation from Jilin University, Changchun, China, in 2021. He is currently working toward the Ph.D. degree in electrical engineering with Xi'an Jiaotong University, Xi'an, China.

His research interests include sequence impedance modeling, control, and stability analysis of power electronic in power systems.

Quanle Zhu was born in Hebei, China, in 1983. He received the Ph.D. degree in electrical engineering from North China Electric Power University, Beijing, China, in 2012.

He is currently a Senior Engineer with State Grid Economic and Technological Research Institute Co., Ltd., Beijing. His main research interest includes HVdc technology.

Yinglin Xue (Member, IEEE) was born in Hebei, China, in April 1986. He received the Ph.D. degree in electrical engineering from Zhejiang University, Hangzhou, China, in 2014.

He is currently a Senior Engineer with State Grid Economic and Technological Research Institute Co., Ltd., Beijing, China. His main research interest includes HVdc technology.

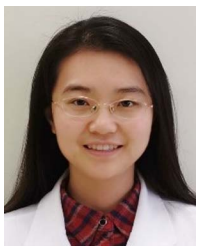

Xuan Li (Member, IEEE) was born in Jiangsu, China, in 1989. She received the B.S. degree from Xi'an Jiaotong University, Shaanxi, China, in 2011, and the M.S. degree from Tsinghua University, Beijing, China, in 2013, both in electrical engineering.

She is currently a Senior Engineer with State Grid Economic and Technological Research Institute, Beijing, China. Her main research interests include VSC-HVdc and LCC-HVdc system design, as well as renewable energy integration.

Bole Feng received the B.S. degree in electrical engineering and automation from the Guangdong University of Technology, Guangzhou, China, in 2020. He is currently working toward the M.S. degree in electrical engineering with Xi'an Jiaotong University, Xi'an, China.

His research interests include the modeling and control of modular multilevel converters and HVdc.

Runtian Li was born in Hebei, China, in 1998. He received the B.S. degree in electrical engineering from Southwest Jiaotong University, Chengdu, China, in 2020. He is currently working toward the Ph.D. degree in electrical engineering with Xi'an Jiaotong University, Xi'an, China.

His research interests include MMC-HVdc, power quality, and the applications of power electronics in power systems.